



University of Ljubljana

Faculty of Mathematics and Physics

## **THERMAL HYDRAULIC DESIGN OF IRRADIATION FACILITY BASED ON O-16 (N,P) N-16 ACTIVATION IN TRIGA REACTOR**

University of Ljubljana – Faculty of Math and Physics

Lappeenranta–Lahti University of Technology LUT

Erasmus Mundus Joint Master's Degree in Safe and Reliable Nuclear Application:

Nuclear Reactor Operation and Safety Track, Master's Thesis

2022

Bernadeth Amano

Adviser: Assist. Prof. DSc Boštjan Končar, University of Ljubljana

Co-Advisor: Dr. Heikki Suikkanen, Lappeenranta-Lahti University of Technology LUT

## ABSTRACT

University of Ljubljana – Faculty of Math and Physics

Lappeenranta–Lahti University of Technology LUT

Bernadeth Amano

### **Thermal hydraulic design of irradiation facility based on O-16 (n,p) N-16 activation in TRIGA reactor**

Master's thesis

2022

90 pages, 46 figures, 16 tables and 4 appendices

Adviser: Assist. Prof. DSc Boštjan Končar

Co-Advisor: Dr. Heikki Suikkanen

**Keywords:** CFD analysis, water activation, irradiation facility, TRIGA

Water, typically used as the primary coolant in facilities such as fusion and fission reactors, could be exposed to a large amount of neutrons causing water activation. This phenomenon could cause radiation damage to electrical components and increase the dose to personnel. As there are only few sources of gamma rays with energies in the range of 6 MeV and 7 MeV, an irradiation system using activated cooling water as a source of energetic gamma rays is proposed at the Jozef Stefan Institute (JSI) TRIGA Mark II research reactor. A water activation irradiation loop design is proposed, inserted into a radial piercing port of a research reactor. In this thesis, a numerical model of the irradiation loop was developed and a CFD analysis was performed using ANSYS CFX. Pressure and velocity profiles were established and will serve as design limits and criteria reference for assembling the actual facility. Moreover, the  $^{16}\text{N}$  concentration inside the loop was studied. Its formation and decay inside the loop were predicted. This shall serve as reference for future experimental designs and further studies to be conducted using the proposed facility.

UNIVERZA V LJUBLJANI  
FAKULTETA ZA MATEMATIKO IN FIZIKO  
ODDELEK ZA FIZIKO  
JEDRSKA TEHNIKA

LAPPEENRANTA-LAHTI UNIVERSITY OF TECHNOLOGY  
LUT  
SCHOOL OF ENERGY SYSTEMS  
NUCLEAR ENGINEERING

Bernadeth Luzares Amano

**TERMO-HIDRAVLICNA ZASNOVA  
OBSEVALNE ZANKE Z AKTIVACIJO O-16 (N,P)  
N-16 V TRIGA REAKTORJU**

MAGISTRSKO DELO

MENTOR: Doc. Dr. Boštjan Končar  
SOMENTOR: Dr. Heikki Suikkanen

Ljubljana, 2022



## Acknowledgement

I would like to thank my adviser, Assist. Prof. DSc. Boštjan Končar for his thorough guidance, support, and insightful advice throughout the writing of this thesis. I am also thankful for the valuable comments from DSc. Heikki Suikkanen. My utmost gratitude to Anil Kumar Basavaraj for generously sharing his time and CFD expertise; to DSc. Matej Tekavčič for imparting his knowledge on including additional variable on CFX; to Domen Kotnik for answering the queries I may had related to his current study. I would also like to express my gratitude to Prof. DSc. Iztok Tiselj for his guidance and support. Lastly, I thank everyone who, in one way or another, have contributed to this study. I also acknowledge the Erasmus Mundus Safe and Reliable Nuclear Applications program, I would not be able to undertake this study without their scholarship support.



# **Thermal hydraulic design of irradiation facility based on O-16 (n,p) N-16 activation in TRIGA reactor**

## **ABSTRACT**

Water, typically used as the primary coolant in facilities such as fusion and fission reactors, could be exposed to a large amount of neutrons causing water activation. This phenomenon could cause radiation damage to electrical components and increase the dose to personnel. As there are only few sources of gamma rays with energies in the range of 6 MeV and 7 MeV, an irradiation system using activated cooling water as a source of energetic gamma rays is proposed at the Jozef Stefan Institute (JSI) TRIGA Mark II research reactor. A water activation irradiation loop design is proposed, inserted into a radial piercing port of a research reactor. In this thesis, a numerical model of the irradiation loop was developed and a CFD analysis was performed using ANSYS CFX. Pressure and velocity profiles were established and will serve as design limits and criteria reference for assembling the actual facility. Moreover, the  $^{16}\text{N}$  concentration inside the loop was studied. Its formation and decay inside the loop were predicted. This shall serve as reference for future experimental designs and further studies to be conducted using the proposed facility.

**Keywords:** CFD analysis, water activation, irradiation facility, TRIGA





# Termo-hidravlična zasnova obsevalne zanke z aktivacijo O-16 (n,p) N-16 v TRIGA reaktorju

## POVZETEK

Voda s katero običajno hladimo fuzijske in fisijske reaktorje je lahko izpostavljena večji količini nevtronov in se pri tem aktivira. Sevanje zaradi aktivacije vode lahko povzroči poškodbe električnih komponent in poveča prejeto dozo za osebe. Ker obstaja le malo virov gama žarkov z energijami v območju med 6 MeV in 7 MeV, za preučevanje pojava na raziskovalnem reaktorju TRIGA Mark II na Institutu »Jožef Stefan« predlagajo obsevalni sistem z uporabo aktivirane vode kot vira gama žarkov. Predlagana je zasnova obsevalne zanke, ki je vstavljena v radialno odprtino raziskovalnega reaktorja. V tem magistrskem delu smo razvili numerični model obsevalne zanke in izvedli analizo s pomočjo programa za računalniško dinamiko tekočin (RDT) ANSYS CFX. Izračunali smo porazdelitve tlaka in hitrosti, ki bodo služile kot projektna osnova za dejansko izdelavo obsevalne zanke. Poleg tega smo proučevali obnašanje koncentracije izotopa dušika  $^{16}\text{N}$  v zanki. Pri tem smo upoštevali njegov nastanek in razpad znotraj zanke. Izračunane koncentracije dušika  $^{16}\text{N}$  bodo služile kot referenca za prihodnje zasnove eksperimentov in nadaljnje študije v predlagani obsevalni napravi.

**Ključne besede:** RDT analiza, aktivacija vode, obsevalna zanka, TRIGA



# Contents

<b>List of figures</b>	<b>13</b>
<b>List of tables</b>	<b>15</b>
<b>List of abbreviations and symbols</b>	<b>17</b>
<b>1 Introduction</b>	<b>19</b>
1.1 Background of the study	19
1.2 Objectives	20
1.2.1 General Objectives	20
1.2.2 Specific Objectives	20
<b>2 Theoretical Background</b>	<b>21</b>
2.1 Water Activation	21
2.2 Primary Coolant Activation Calculation	22
<b>3 TRIGA Reactor</b>	<b>25</b>
<b>4 Conceptual design of the water activation loop</b>	<b>27</b>
<b>5 Fluid dynamics</b>	<b>31</b>
5.1 Governing equations	31
5.2 Transport equation for additional variables	32
<b>6 Methodology: The CFD modelling process</b>	<b>35</b>
6.1 Geometry of the irradiation loop	35
6.2 Mesh generation	37
6.3 CFD solver process	41
6.3.1 Boundary conditions	41
6.3.2 Flow model	42
6.3.3 Solution procedure	43
6.3.4 Post-processing	44
<b>7 Inclusion of the transport equation for <math>^{16}\text{N}</math></b>	<b>45</b>
7.1 Loading the reaction rates	46
7.2 Transport equation for a passive scalar	47
7.2.1 ANSYS CFX expressions for additional terms	49
<b>8 Results and discussion</b>	<b>51</b>
8.1 $^{16}\text{N}$ concentration	55

<b>9</b>	<b>Verification</b>	<b>65</b>
9.1	Residuals and imbalances	65
9.2	Additional variable imbalance	65
9.3	Comparison with the FLUENT results	67
9.4	$^{16}\text{N}$ estimation	69
<b>10</b>	<b>Conclusions</b>	<b>71</b>
<b>11</b>	<b>Recommendations</b>	<b>73</b>
	<b>Bibliography</b>	<b>75</b>
	<b>Appendix A Model Dimensions</b>	<b>77</b>
	<b>Appendix B Mesh Settings</b>	<b>79</b>
	<b>Appendix C Residuals</b>	<b>85</b>
	<b>Appendix D Additional Variable Imbalance</b>	<b>87</b>
	<b>Razširjeni povzetek v slovenskem jeziku</b>	<b>89</b>

# List of figures

3.1	Side View of the TRIGA Reactor [1]. . . . .	25
3.2	Top View of the TRIGA Reactor [1]. . . . .	26
4.1	Schematic drawing of the JSI TRIGA reactor core [2]. . . . .	28
4.2	Model of the basic conceptual design of the water activation loop in radial piercing port. . . . .	29
6.1	Irradiation loop geometry. . . . .	36
6.2	Side view of irradiation loop snail part. . . . .	36
6.3	Isometric view of irradiation loop snail part. . . . .	37
6.4	Mesh of the modelled irradiation loop. . . . .	38
6.5	$y^+$ values along the loop for SST model with automatic wall function. . . . .	40
6.6	Data sample locations for $y^+$ values. . . . .	40
6.7	Inlet and outlet locations. . . . .	42
7.1	Reaction rate map for JSI TRIGA (in $cm^{-3}s^{-1}$ [3]. . . . .	46
7.2	Normalized reaction rates [ $m^{-3}s^{-1}$ ] for TRIGA reactor at full power of 250 kW. . . . .	48
8.1	Pressure profile results. . . . .	52
8.2	Pressure profile results in the snail part. . . . .	53
8.3	Velocity distribution. . . . .	54
8.4	Velocity profile results at inlet and outlet boundaries. . . . .	54
8.5	Velocity profile results at various viewing angle. . . . .	56
8.6	$^{16}N$ concentration profile results from stage 1. . . . .	57
8.7	$^{16}N$ concentration profile results at snail from stage 1. . . . .	58
8.8	$^{16}N$ concentration profile results from stage 1, view adjacent to reactor core. . . . .	59
8.9	$^{16}N$ concentration profile results from stage 2 (decay on mirror loop). . . . .	60
8.10	$^{16}N$ concentration profile results at snail from stage 2 (decay on mirror loop). . . . .	60
8.11	$^{16}N$ concentration profile results from stage 2 (decay on mirror loop), view adjacent to reactor core. . . . .	61
8.12	$^{16}N$ concentration profile results from stage 3. . . . .	62
8.13	$^{16}N$ concentration profile results at snail from stage 3. . . . .	63
8.14	$^{16}N$ concentration profile results at snail from stage 3. Side view. . . . .	64
8.15	$^{16}N$ concentration profile results from stage 3, view adjacent to reactor core. . . . .	64
9.1	$N_{max}$ plot for simulation at 20000 iterations. . . . .	66

9.2	Pressure distribution results from FLUENT (left) and ANSYS CFX (right). . . . .	67
9.3	Comparison of velocity distributions between FLUENT (left) and ANSYS CFX (right). . . . .	68
9.4	Velocity profile results in the snail part from FLUENT (left) vs ANSYS CFX (right). . . . .	68
9.5	Velocity profile results at inlet and outlet boundaries from FLUENT (left) vs ANSYS CFX (right). . . . .	69
A.1	Dimension of whole body. . . . .	77
A.2	Baffle dimensions. . . . .	77
A.3	Snail dimensions. . . . .	78
B.1	Ideal and skewed triangles and quadrilaterals [4]. . . . .	80
B.2	Percent mesh volume of entire model vs skewness ( <i>Tet4 = 4 Node Linear Tetrahedron; Wed6 = 6 Node Linear Wedge [Prism]</i> ). . . . .	81
B.3	Location of bad (sliver) mesh cell with maximum skewness. . . . .	81
B.4	Percent mesh volume of entire model vs orthogonal quality ( <i>Tet4 = 4 Node Linear Tetrahedron; Wed6 = 6 Node Linear Wedge [Prism]</i> ). . . . .	82
B.5	Number of elements vs orthogonal quality for cells below orthogonal quality value limit of 0.15 ( <i>Tet4 = 4 Node Linear Tetrahedron; Wed6 = 6 Node Linear Wedge [Prism]</i> ). . . . .	83
B.6	Location of mesh cells with orthogonal values below the limit ( $<0.15$ ). . . . .	83
C.1	Residuals plot for simulation at 1000 iterations. . . . .	85
C.2	Residuals plot for simulation at 8000 iterations. . . . .	86
D.1	Imbalance plot for N at 1000 (left) and at 3000 (right) iterations. . . . .	87
D.2	Imbalance plot for N at 5000 (left) and at 8000 (right) iterations. . . . .	87
D.3	Imbalance plot for N at 10000 (left) and at 13000 (right) iterations. . . . .	88
D.4	Imbalance plot for N at 15000 (left) and at 20000 (right) iterations. . . . .	88
11.5	Porazdelitev tlaka v simulirani polovici zanke. . . . .	90
11.6	Porazdelitev hitrosti v simulirani polovici zanke. . . . .	90
11.7	Porazdelitev koncentracije dušika $^{16}\text{N}$ v simulirani polovici zanke. . . . .	90

# List of tables

2.1	Activation reactions data [5]. . . . .	21
6.1	Mesh characteristics. . . . .	39
6.2	Boundary Conditions . . . . .	42
6.3	Details of SOLVER CONTROL. . . . .	43
7.1	MCNP reaction rate normalization terms. . . . .	47
7.2	Basic settings for additional variable $N$ . . . . .	48
7.3	Constants for additional variable [5][6] . . . . .	50
8.1	Summary of steady-state simulation results. . . . .	51
8.2	Boundary conditions for additional variable $N$ . . . . .	55
9.1	Additional variable imbalance. . . . .	66
9.2	Results for irradiation loop simulation with FLUENT vs ANSYS CFX. . . . .	67
9.3	$^{16}\text{N}$ estimation parameters. . . . .	70
9.4	Results for $^{16}\text{N}$ decay calculation. . . . .	70
B.1	Results for $^{16}\text{N}$ decay calculation. . . . .	79
B.2	Skewness values and cell quality [4]. . . . .	81
B.3	Orthogonal Quality Limits [4]. . . . .	82





# List of abbreviations and symbols

## Abbreviations

<i>CFD</i>	Computational Fluid Dynamics
<i>JSI</i>	Jozef Stefan Institute

## Symbols

*Note: Some dimensions are given in terms of the fundamental magnitudes of length ( $L$ ), mass ( $M$ ), and time ( $t$ ).*

$A$	activity (Bq)
$D_{\Phi}$	kinematic diffusivity ( $L^2t^{-1}$ )
$E$	fission energy (J or $L^2t^{-2}$ )
$h$	specific enthalpy ( $L^2t^{-1}$ )
$h_{tot}$	specific total enthalpy ( $L^2t^{-1}$ )
$N_o$	number density of target elements in the coolant ( $L^{-3}$ )
$N_o^m$	Stage 2 outlet concentration ( $L^{-3}$ )
$N_2^i$	Stage 1 outlet/ stage 2 inlet concentration ( $L^{-3}$ )
$P$	power (W)
$p$	pressure ( $Pa$ or $ML^{-1}t^{-2}$ )
$R$	average reaction rate ( $L^{-3}t^{-1}$ )
$S_E$	energy source ( $ML^{-1}t^{-3}$ )
$S_M$	momentum source ( $ML^{-2}t^{-2}$ )

$S_\varphi$	volumetric source term, with units of conserved quantity per unit volume per unit time
$t_i$	exposure time in the reactor core (t)
$t_f$	the transit time from the reactor core to the irradiation facility (t)
$T$	total circulation time of the proposed closed water loop system (t)
$\mathbf{U}$	vector of velocity ( $L\ t^{-1}$ )
$v$	neutron per fission
$\sigma_i(E)$	microscopic cross section of the nuclide for reaction i ( $L^2$ )
$\phi(r, E)$	energy dependent neutron flux or neutron spectrum in the primary cooling water (neutron $L^{-2}t^{-1}$ )
$\Phi$	additional variable ( $ML^{-3}$ )
$\varphi$	conserved quantity per unit mass
$\rho$	mixture density $ML^{-3}$ )
$\lambda$	decay constant ( $s^{-1}$ )
$\overline{\overline{\tau}}$	stress tensor ( $ML^{-1}t^{-2}$ )
$\mu$	dynamic viscosity ( $ML^{-1}t^{-1}$ )
$\tau_w$	surface shear stress ( $ML^{-1}t^{-2}$ )

# Chapter 1

## Introduction

### 1.1 Background of the study

Water is typically used as the primary coolant in facilities such as fusion and fission reactors. Hence, this water is exposed to a large amount of neutrons which induces water activation. The activation of water produces activation products, some of which have high-energy, specifically  $^{16}\text{N}$  which is an activation product from  $^{16}\text{O}$ . There are other activation products, but  $^{16}\text{N}$  is focused on since its source  $^{16}\text{O}$  has a high natural abundance. This activated water flows through the primary circuit located outside the primary biological shield. Hence, this could expose the workers close to the circuit to high-energy radiation. Moreover, it could also cause radiation damage to electrical components and, in the case of fusion facilities, additional nuclear heating of various cold components such as superconducting coils cooled by liquid helium.

Since most of today's gamma irradiations are performed with  $^{137}\text{Cs}$  (0.662 MeV) or  $^{60}\text{Co}$  (1.1732 MeV and 1.3325 MeV) sources, an irradiation facility with higher-energy gamma rays could lead to a better evaluation of the testing facilities since we would have a higher threshold of measurement. As there are only few sources of gamma rays with energies in the range of 6 MeV and 7 MeV, an irradiation system using activated cooling water as the source of energetic gamma rays is proposed at the Jozef Stefan Institute (JSI) TRIGA Mark II research reactor.

Preliminary studies [7] made a comparison between a central and radial irradiation facility as presented on Chapter 4. The result of the study judged the radial irradiation facility to be the optimal option. This thesis deals with the computational fluid dynamics modelling of the proposed irradiation facility using ANSYS CFX software. The transport equation for  $^{16}\text{N}$  decay is also introduced into the model.

### 1.2 Objectives

The general, as well as the specific objectives that have been set to carry out the following work at the TRIGA Reactor in the JSI are indicated below.

#### 1.2.1 General Objectives

The main objective of the study is to perform a CFD analysis of the proposed new water activation/irradiation loop for the TRIGA reactor using ANSYS CFX. The results of the CFD analysis will establish the design limits and criteria for assembling the actual facility and will serve as reference for future experimental designs and further activities to be conducted using the proposed facility.

#### 1.2.2 Specific Objectives

- To establish a reliable CFD model of the loop.
- To model the  $^{16}\text{N}$  concentration in the proposed irradiation loop by inserting an additional transport equation for  $^{16}\text{N}$  using ANSYS CFX.
- To verify the simulation results by checking acceptance criteria such as mesh quality, convergence, imbalances, etc. and by comparing the results with available simulation results using FLUENT.

# Chapter 2

## Theoretical Background

The following sections provide a theoretical background regarding the phenomenon being studied involving water activation.

### 2.1 Water Activation

Most nuclear reactors use water as a coolant. Primary water activation could happen even in pure water. The phenomenon occurs when water gets activated by exposure to neutron flux and gamma rays are detected from the water. There are three isotopes of oxygen that could be activated –  $^{16}\text{O}$ ,  $^{17}\text{O}$ , and  $^{18}\text{O}$ . The main nuclides, which contribute to the radioactivity of water, are the  $^{16}\text{N}$  and  $^{18}\text{O}$ , both of which are generated by activation of oxygen isotopes. A small percentage of water gets activated via the  $^{17}\text{O}$  (n,p)  $^{17}\text{N}$  reaction. The data about all the three activation reactions are gathered in the following table:

Table 2.1: Activation reactions data [5].

Isotope	Isotope abundance [%]	Reaction	Activation product	$t_{1/2}$ [s]	Energy of the decay products [MeV]
$^{16}\text{O}$	99.76	(n,p)	$^{16}\text{N}$	7.13	6.13 (gamma ray) and 7.11 (gamma ray)
$^{17}\text{O}$	0.04	(n,p)	$^{17}\text{N}$	4.14	0.38 (neutron) and 1.17 (neutron)
$^{18}\text{O}$	0.20	(n, $\gamma$ )	$^{19}\text{O}$	26.9	0.197 (gamma ray) and 1.357 (gamma ray)

Looking at their isotopic abundances, we know that the most prevalent one is  $^{16}\text{O}$ . The main reaction involves isotope  $^{16}\text{O}$  and its activation product  $^{16}\text{N}$  at energies 6.13 MeV and 7.11 MeV. The (n,p) reaction occurs when a neutron enters a nucleus and a proton leaves it simultaneously. After this event, the nucleus remains in an excited state and decays to the ground state by emitting two characteristic gamma rays

## 2.2 Primary Coolant Activation Calculation

The activation of a nuclide in a reactor is calculated as [8]:

$$R_i(\vec{r}) = \int_0^\infty N_0 \sigma_i(E) \phi(\vec{r}, E) dE, \quad (2.1)$$

where  $N_0$  is the number density of the target elements in the coolant,  $\sigma_i(E)$  is the microscopic cross section of the nuclide for reaction  $i$  and  $\phi(\vec{r}, E)$  is the energy dependent neutron flux or neutron spectrum in the primary cooling water.

The change of radionuclide concentration in the primary coolant  $N$  can be described by the following equation [9]:

$$\frac{dN(t)}{dt} = R - \lambda N, \quad (2.2)$$

where  $\lambda$  is the decay constant and  $R$  is the average reaction rate in the region. To calculate the specific activity of the radionuclide, which is the result of activation, the solution for  $N(t)$  needs to be multiplied by the decay constant  $\lambda$ :

$$A(t) = N(t) \lambda = R (1 - e^{-\lambda t}), \quad (2.3)$$

After a long exposure the activity reaches saturation  $A = R = N_0 \sigma \varphi$

However, the water in the loop system circulates and is exposed to the neutron flux in the reactor core for a short period of time, in the order of seconds [10]. Thus, the activity of the activated water at the inlet to the irradiation facility is described by the equation [2]:

$$a_i = R \frac{1 - e^{-\lambda t_i}}{1 - e^{-\lambda T}} e^{-\lambda t_f}, \quad (2.4)$$

## 2.2. Primary Coolant Activation Calculation

---

where  $t_i$  is the exposure time in the reactor core,  $T$  is the total circulation time of the proposed closed water loop system and  $t_f$  is the transit time from the reactor core to the irradiation facility.





## Chapter 3

### TRIGA Reactor

This chapter discusses the basic technical and operational characteristics of the TRIGA (Training, Research, Isotopes, General Atomics) Mark II reactor at the Jožef Stefan Institute (JSI), which has been in operation since 1966. The reactor is a typical 250 kW TRIGA Mark II light-water reactor with an annular graphite reflector cooled by natural convection. The side and top views of the reactor are shown in Figures 3.1 and 3.2 [1].

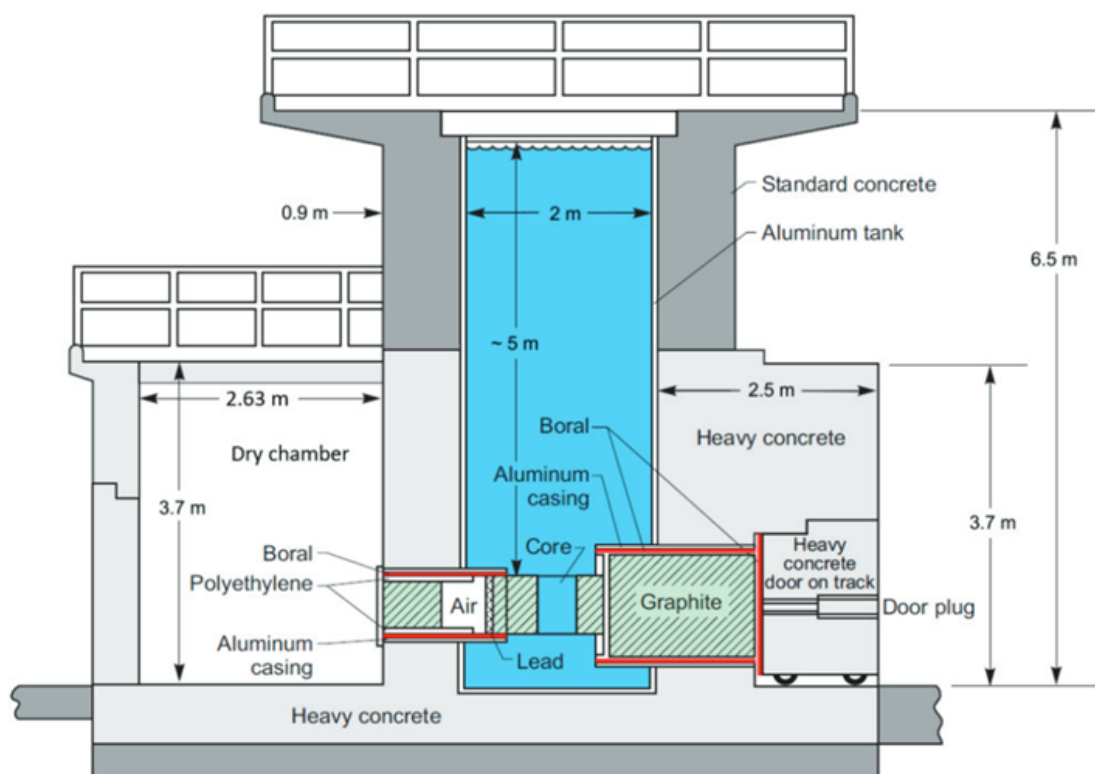


Figure 3.1: Side View of the TRIGA Reactor [1].

The core is placed at the bottom of the 6.25 m-high open tank with a diameter of 2 m. The core has a cylindrical configuration (Figure 4.1). In total, there are 91 locations in the core, that can be filled either by fuel elements or other components like control rods, neutron source, irradiation channels, etc. The fuel is a homoge-

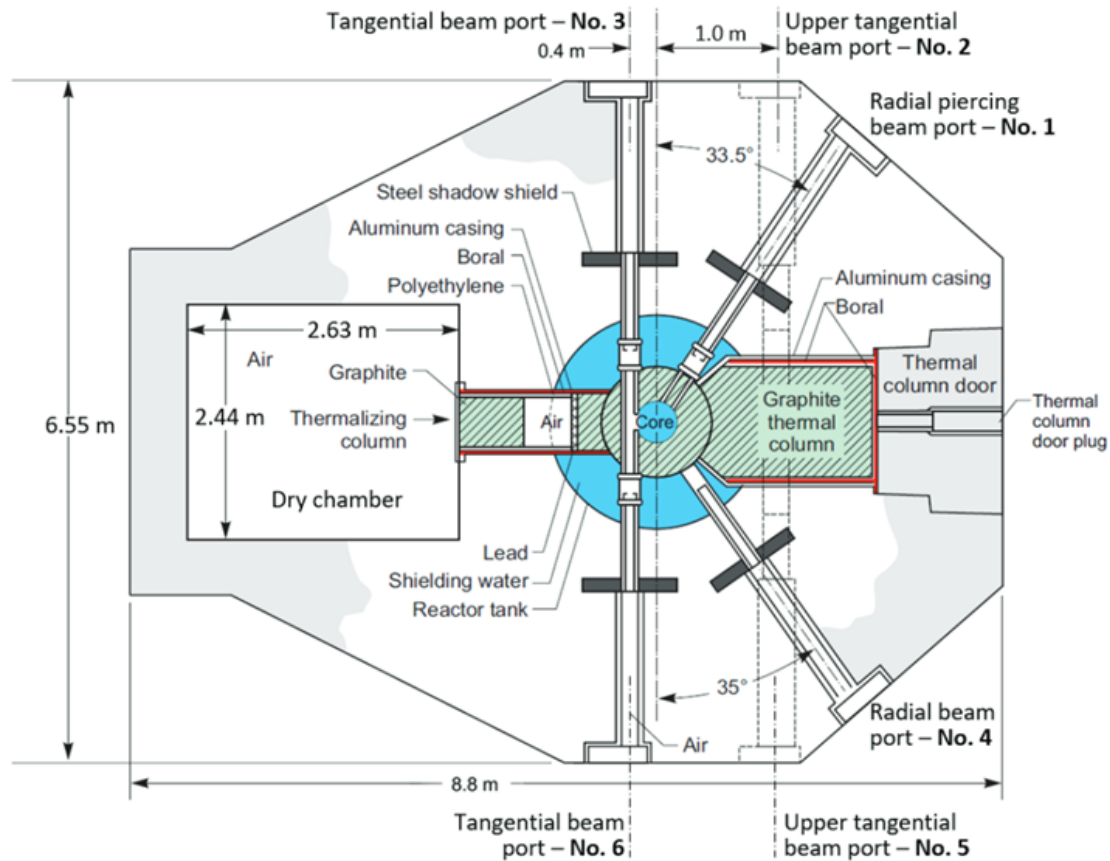


Figure 3.2: Top View of the TRIGA Reactor [1].

neous mixture of uranium and zirconium hydride with 12 wt.% uranium with 20% enrichment (uranium is 20 wt.%  $^{235}\text{U}$ ).

Three control rods of fueled-follower type are used in the reactor: regulating (R), shim (C), and safety (S). Their locations are indicated in Figure 4.1. They are identical in geometry and composition. The transient rod is equipped with a pneumatic system for rapid withdrawal. The core is surrounded by a circular graphite reflector.

## Chapter 4

# Conceptual design of the water activation loop

The irradiation channels of JSI TRIGA are located in the outermost positions of the core with one extra channel at the central position of the reactor core. There are also three horizontal irradiation channels, i.e. two radial and one tangential, penetrating the concrete structure of the reactor.

A preliminary study [2] was conducted assessing two conceptual designs, one utilizing a central irradiation channel and one utilizing a radial piercing port for water activation. For a radial piercing port, the facility consists of a pipe loop inserted into it wherein the pipes with the activated water will be guided outside of the port directly to the irradiation facility next to the port opening (Figures 4.1 and 4.2). The central irradiation channel, on the other hand, will consist of pipes guided through the reactor tank to the reactor platform and then back down to the ground floor.

The conceptual design utilizing the radial piercing was chosen as the best option due to the simpler design of the irradiation loop, already present shielding of the loop and comparable  $^{16}\text{N}$  decay rates in the irradiation facility. Since the water activation is in saturation in the proposed design, small changes in water flow rate will have little effect on the  $^{16}\text{N}$  decay rate in the irradiation facility compared to the conceptual design utilizing a central channel.

One of the radial ports ends on the outside of the graphite reflector, while the other, namely the radial piercing port, penetrates the graphite reflector and reaches the reactor core. The latter port was therefore chosen as the main candidate for the installation of the closed-water loop due to the much higher neutron flux causing a higher activation rate of water.

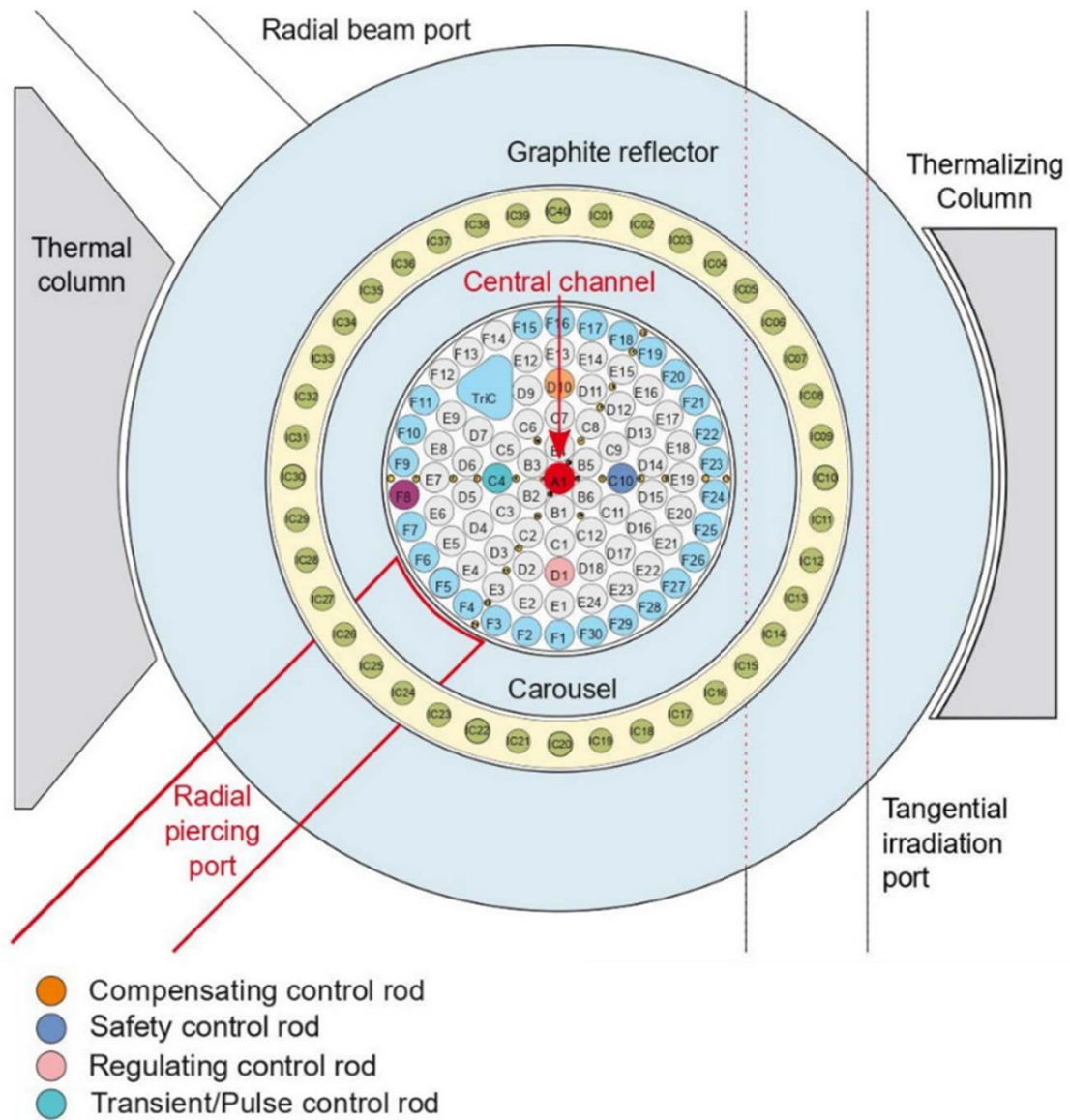


Figure 4.1: Schematic drawing of the JSI TRIGA reactor core [2].

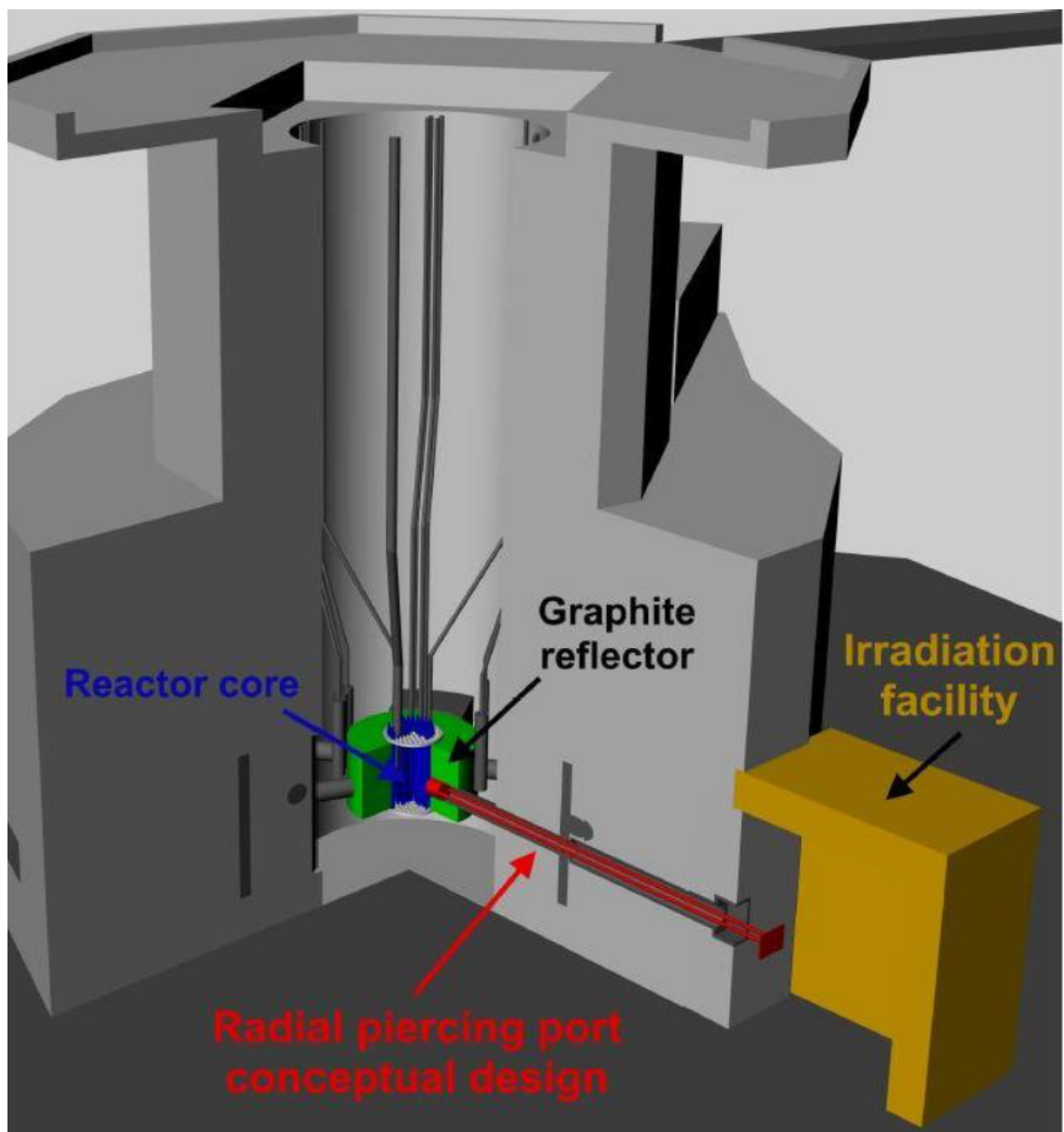


Figure 4.2: Model of the basic conceptual design of the water activation loop in radial piercing port.



# Chapter 5

## Fluid dynamics

Computational Fluid Dynamics (CFD) is the use of computers in solving the governing equations of physical phenomena involving fluid dynamics and heat transfer problems. This chapter discusses the theory behind the CFD tool utilized in this study, namely ANSYS CFX.

### 5.1 Governing equations

Fluid Dynamics is a branch of fluid mechanics that deals with fluid motion, i.e. fluid flow and the effect of forces on it. Fluid flow is described by the governing equations, i.e. the Navier-Stokes equations which describe how the velocity, pressure, temperature and density of fluid flow are related.

The governing equations in CFD include the following conservation laws of physics:

- Conservation of mass
- Newton's second law: the change of momentum equals the sum of forces on a fluid particle.
- First law of thermodynamics (conservation of energy): rate of change of energy equals to the sum of rate of heat addition to a fluid particle and the work done on it.

The set of equations solved by ANSYS CFX [8] are the unsteady Navier-Stokes equations in their conservation form. The instantaneous equations of mass, momentum and energy conservation can be written as follows:

*the continuity equation*

$$\frac{\partial \rho}{\partial t} + \nabla \cdot (\rho \mathbf{U}) = 0, \quad (5.1)$$

where:

- $\mathbf{U}$  is the fluid velocity vector
- $\rho$  is the fluid density

*the momentum equations*

$$\frac{\partial(\rho\mathbf{U})}{\partial t} + \nabla \cdot (\rho\mathbf{U} \otimes \mathbf{U}) = -\nabla p + \nabla \cdot \bar{\bar{\tau}} + S_M, \quad (5.2)$$

where  $S_M$  is the momentum source and the stress tensor,  $\bar{\bar{\tau}}$ , is related to the strain rate by:

$$\bar{\bar{\tau}} = \mu(\nabla\mathbf{U} + (\nabla\mathbf{U})^T) - \frac{2}{3}\delta\nabla \cdot \mathbf{U}, \quad (5.3)$$

*and the total energy equation*

$$\frac{\partial(\rho h_{tot})}{\partial t} - \frac{\partial\rho}{\partial t} + \nabla \cdot (\rho\mathbf{U}h_{tot}) = \nabla \cdot (\lambda\nabla T) + \nabla \cdot (\mathbf{U} \cdot \bar{\bar{\tau}}) + \mathbf{U} \cdot S_M + S_E, \quad (5.4)$$

where  $S_E$  is the energy source and  $h_{tot}$  is the total enthalpy, related to the static enthalpy  $h(T, p)$  by:

$$h_{tot} = h + \frac{1}{2}U^2, \quad (5.5)$$

The term  $\nabla \cdot (\mathbf{U} \cdot \bar{\bar{\tau}})$  represents the work due to viscous stresses and is called the viscous work term. This models the internal heating by viscosity in the fluid, and is negligible in most flows. The term  $\mathbf{U} \cdot S_M$  represents the work due to external momentum sources and is currently neglected.

## 5.2 Transport equation for additional variables

Additional variables are non-reacting, scalar components that are transported through the flow, or through the solid (including the solid portion of the porous domain). They can be used to model, for example, the distribution of dye through a liquid, or smoke from a fire. ANSYS CFX typically interprets additional variables as concentrations within the fluid domain. Additional variables can be set up as algebraic equations, Poisson equations, or transport equations.



The general form of the transport equation for the additional variable is [11]:

$$\frac{\partial (\rho\varphi)}{\partial t} + \nabla \cdot (\rho \mathbf{U} \varphi) = \nabla \cdot (\rho D_\Phi \nabla \varphi) + S_\varphi, \quad (5.6)$$

where:

- $\mathbf{U}$  is the fluid velocity vector in the case of a fluid or porous domain, or  $U \equiv U_s$  in the case of a solid domain with a specified velocity of solid motion, where  $U_s$  is the solid velocity.
- $\rho$  is the mixture density, mass per unit volume
- $\Phi$  is the conserved quantity per unit volume, or concentration
- $\varphi = \Phi/\rho$  is the conserved quantity per unit mass
- $S_\varphi$  is a volumetric source term, with units of conserved quantity per unit volume per unit time
- $D_\Phi$  is the kinematic diffusivity for the scalar



# Chapter 6

## Methodology: The CFD modelling process

For this study, an optimal model [9] for the proposed radial irradiation loop was provided from the ongoing study. CFD analysis with FLUENT were performed with various models and considerations to come up with the final design as used in this thesis.

### 6.1 Geometry of the irradiation loop

The provided Computer Aided Design (CAD) drawing is first imported as geometry in the ANSYS Workbench. This model initially consists of various parts that could make meshing more complicated by producing unnecessary high number of control volumes, leading to longer calculation time. Moreover, defining boundary conditions using the crude CAD geometry, not adapted for CFD analysis, would be more difficult, potentially leading to errors. Hence, using the Spaceclaim feature of ANSYS [12], the CAD geometry parts can be corrected to ensure clean geometry edges and surfaces and combined into one simple form.

Figure 6.1 presents the CAD irradiation loop geometry. The model consists of a snail part and a pipe part as referred in this study. The snail part is indicated in Figure 6.1 with the remaining being the pipe part. This irradiation loop represents just half of the proposed irradiation loop design. The other half had the exact geometry, referred in this text as the mirror loop, and is connected at the inlet and outlet pipes. The first half of the irradiation loop as presented here is distinguished such that it is located close to the reactor core with the mirror loop directly connected to it as in Figure 4.2. As both parts identical with the exception of radiation presence, only half of the irradiation loop was simulated to avoid long simulation times.

Using the Design Modeler feature of ANSYS, the fluid and solid domain of the model was defined. During this stage, the model now consists of two parts which shall be combined into one using the “Form New Part” option. This is done to create a conformal mesh between the two parts, implying that the parts share nodes at the interface of the two parts. The mesh will be continuous across the bodies at the shared face/edge and shared topology feature is activated.

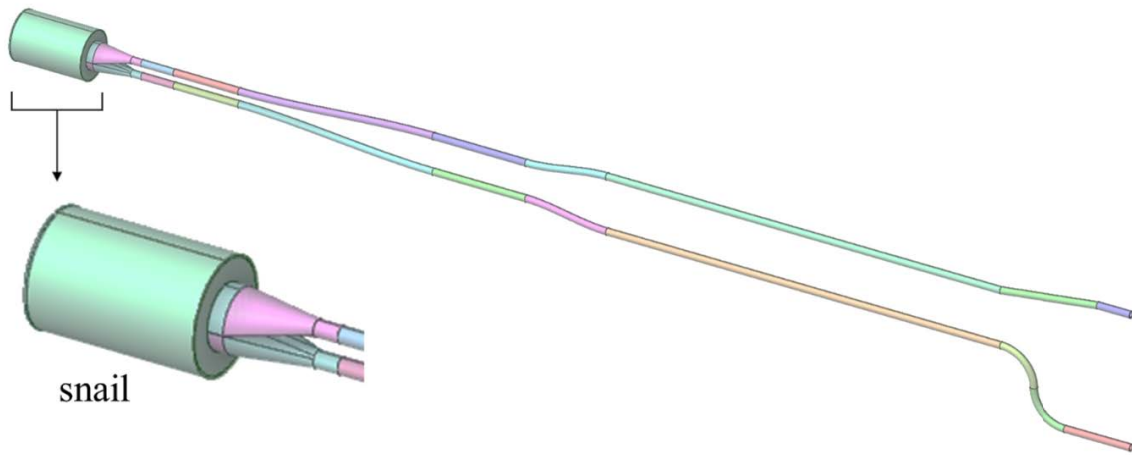


Figure 6.1: Irradiation loop geometry.

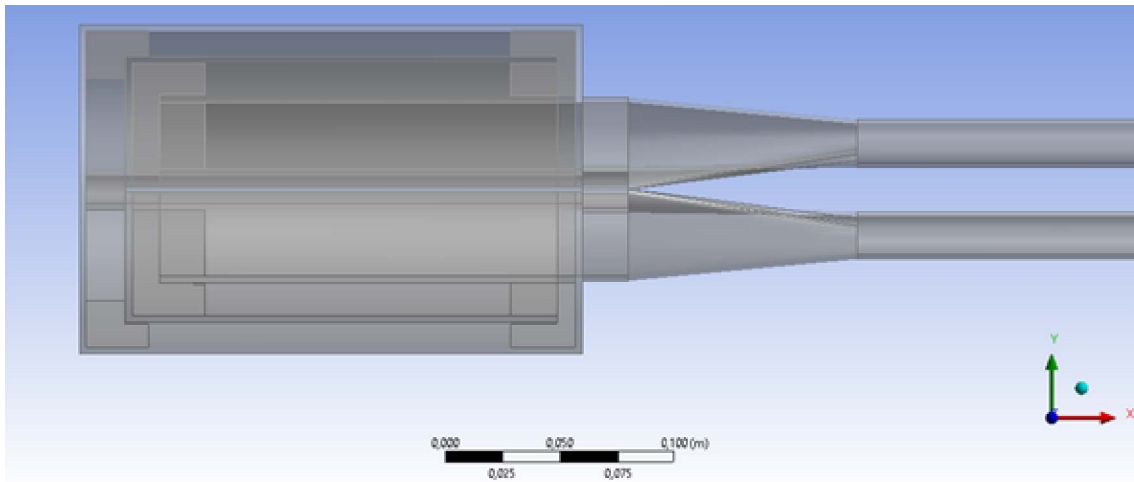


Figure 6.2: Side view of irradiation loop snail part.

Figures 6.2 and 6.3 present the side and isometric view of the snail part of the irradiation loop. This part is the one closest to the reactor core. As the fluid enters the transport pipes, it reaches the snail part, where the fluid flow is slowed down by baffles and structures inside the snail until it reaches the pipe directed to the outlet. Most of the activation processes take place in this part. The fluid is then transported very quickly through the narrow outlet pipe.

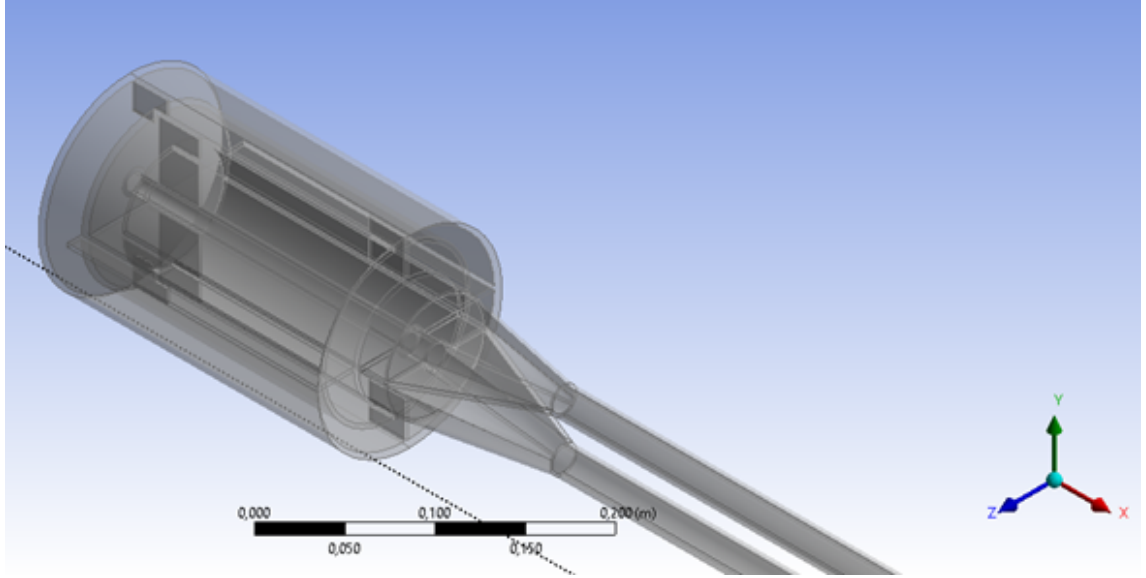


Figure 6.3: Isometric view of irradiation loop snail part.

## 6.2 Mesh generation

The mesh was generated using ANSYS Workbench Meshing tool. The CAD model created beforehand was used. For this study, the focus is on creating an acceptable mesh by analyzing the mesh quality in terms of skewness, and orthogonal quality. Detailed mesh refinement analysis is beyond the scope of this study. Although, to some extent this has been performed in a parallel study using FLUENT [13]. The mesh used here is deemed acceptable based on this previous study. Skewness and orthogonal quality of the selected mesh are discussed in detail in Appendix B.

Figure 6.4 shows the optimized mesh and Table 6.1 shows the mesh characteristics after the meshing procedure. This includes the number of nodes, elements, and mesh metrics. The mesh metrics provides an evaluation of the mesh quality in terms of element quality, skewness, and orthogonal quality, among others. Based on the skewness criteria (Table B.2, the values presented in Table 6.1 are acceptable, with only one problematic cell located at the middle of snail (B.3). The orthogonal value is also acceptable based on the criteria presented on Table (B.3). The location of the cells beyond the limit are very few (less than 360 cells) and are scattered throughout the geometry (Figure B.6). They constitute  $1.34 \times 10^{-4}$  percent of the total mesh volume and are hence deemed negligible. Further details on mesh settings are presented in Appendix B.

First, a relatively coarse mesh was created using ANSYS Mesh default settings, but it ultimately led to convergence issues. This appears to be due to too small cells near the boundary. Hence, bearing the skewness and orthogonal quality limits in mind, an optimized mesh is produced as shown in Figure 6.4. This is done by manual adjustments and trial-and-error method using body sizing and inflation until the criteria is met.

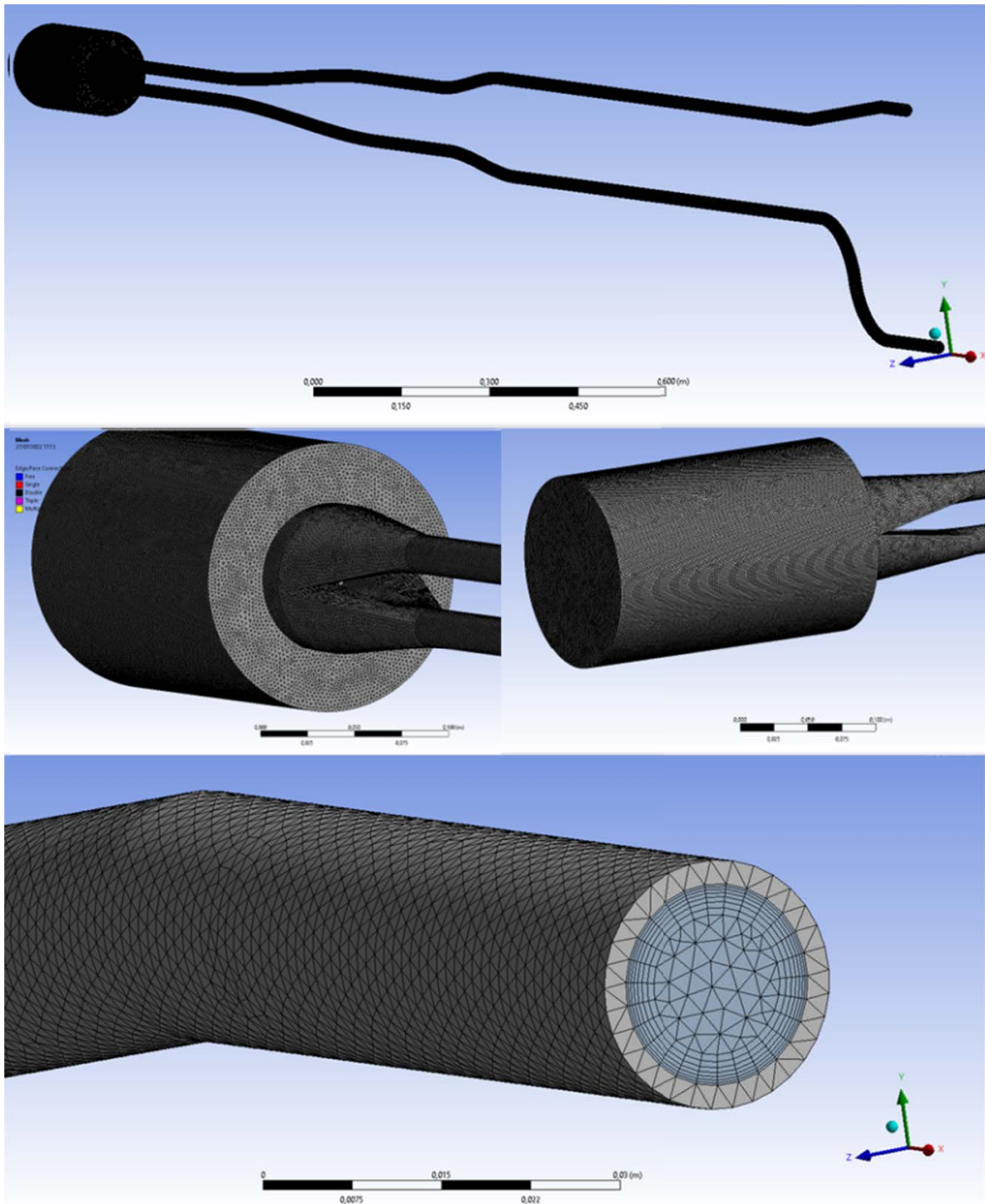


Figure 6.4: Mesh of the modelled irradiation loop.

Table 6.1: Mesh characteristics.

Properties	Value
Skewness	Min: $1.70 \times 10^{-10}$ Max: 0.939 Average: 0.202
Orthogonal Quality	Min: $2.42 \times 10^{-2}$ Max: 0.998 Average: 0.795
Body sizing	Element size: 0.002 m
$y^+$	Min: 8.9 Max: 48.6
Nodes	2432608
Elements	7897492

Body sizing is conducted on the model to provide more control over how the mesh size is distributed within the body. The element size defines the mesh quality. Inflation layers are on the boundary surfaces of the fluid domain. As the velocity gradients normal to the wall are typically much larger than the gradients parallel to the wall, adding an inflation layer creates thinner elements that can resolve and capture the higher wall-normal gradients in the boundary layer. It should be noted that the automatic inflation was turned off before adding the local inflation, as using a mixture of both is not recommended since automatic inflation will ignore all bodies and all attached faces to which local inflation is applied [4]. Further details on the body sizing and inflation control options used herein is described in Appendix B.

#### $y^+$ value

To further assess the quality of the mesh, a metric, dimensionless wall distance  $y^+$  is examined. This value tells how the near-wall element is situated depending on the flow conditions. It is given by the standard definition of  $y^+$  generally used in CFD:

$$y^+ = (u_T \cdot y) / \nu, \quad (6.1)$$

where  $\nu_T$  is the friction velocity defined by  $\sqrt{\frac{\tau_w}{\rho}}$ ,  $y$  is the distance between the first and second grid points off the wall, and  $\nu$  is the kinematic molecular viscosity  $\mu/\rho$ .

Following the settings and parameters which shall be discussed in detail in the

succeeding sections, namely, the use of Shear Stress Transport turbulence model (SST) and automatic wall function, the  $y^+$  values are assessed.

Figure 6.5 presents the  $y^+$  values at selected data points along the loop as shown on Figure 6.6. From Figure 6.5, it shows that the  $y^+$  values along the snail portion is below 11. Outside the snail portion i.e. along the pipe, the  $y^+$  values are above 30 and are mostly on the range of 40 to 50.

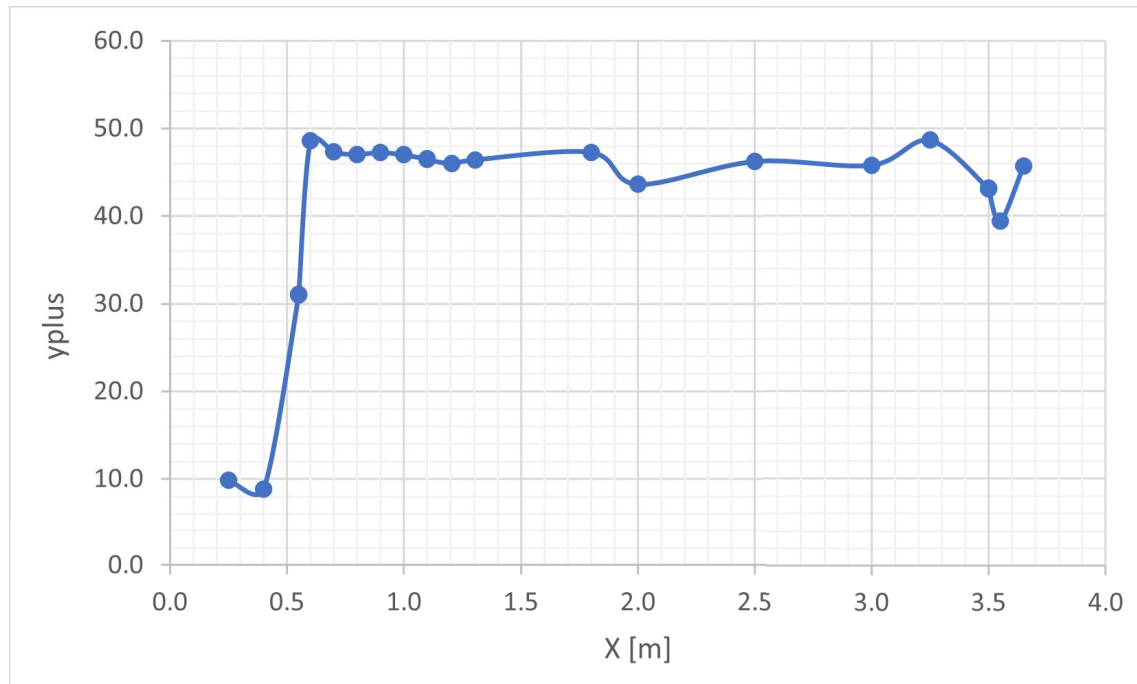


Figure 6.5:  $y^+$  values along the loop for SST model with automatic wall function.

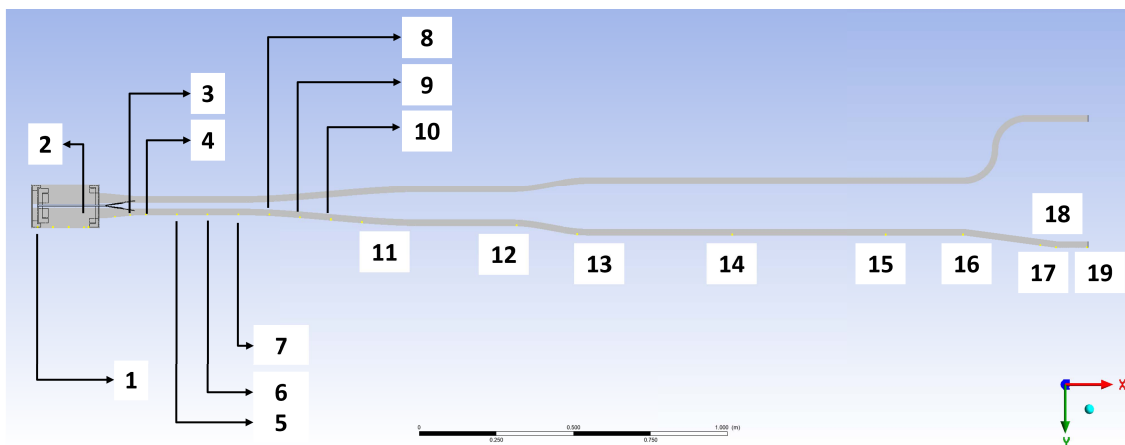


Figure 6.6: Data sample locations for  $y^+$  values.

When directly resolving the viscous sublayer, ideally a value for  $y^+ \sim 1$  would be



required, which will require significantly more mesh elements and effort. This will lead to higher meshing and solution times and the requirement for more computer resources. As this study does not include complex phenomena such as heat transfer, resolving the viscous sublayer is not so important and the use of automatic wall function is adequate. For such case, a  $y^+ > 30$  is valid [14][15]. SST with automatic wall function uses wall functions for  $y^+ > 11$  and transitions to integration to the wall for  $y^+ < 11$  [11].

From Figure 6.5, it could be concluded that the  $y^+$  values calculated are more or less within the acceptable range for the SST model with automatic wall function treatment. Based on this and aforementioned criteria, the mesh is deemed acceptable.

## 6.3 CFD solver process

The following steps are taken in setting up the computation:

- Load the input file containing the previously generated mesh.
- Set up proper boundary conditions.
- Set up the flow model.
- Run the simulation.
- Post process results.

### 6.3.1 Boundary conditions

Following the generation of geometry and mesh, the boundary conditions for the flow are defined. Fluid and solid domains are identified, and a fluid-solid interface is created to distinguish the boundary conditions between these domains. The inlet and outlet locations are also specified.

Relevant boundary conditions are summarized in Table 6.2 and further discussed in the subsequent sections.

The boundary conditions for momentum equation are set up as follows:

- Boundary condition for the fluid velocity on the wall, at the fluid-solid interface, is defined as a no-slip boundary, which means that the fluid velocity at the stationary wall is zero.
- As indicated in Table 6.2, the mass flow is specified at the inlet to the fluid domain, and the pressure boundary at the outlet.

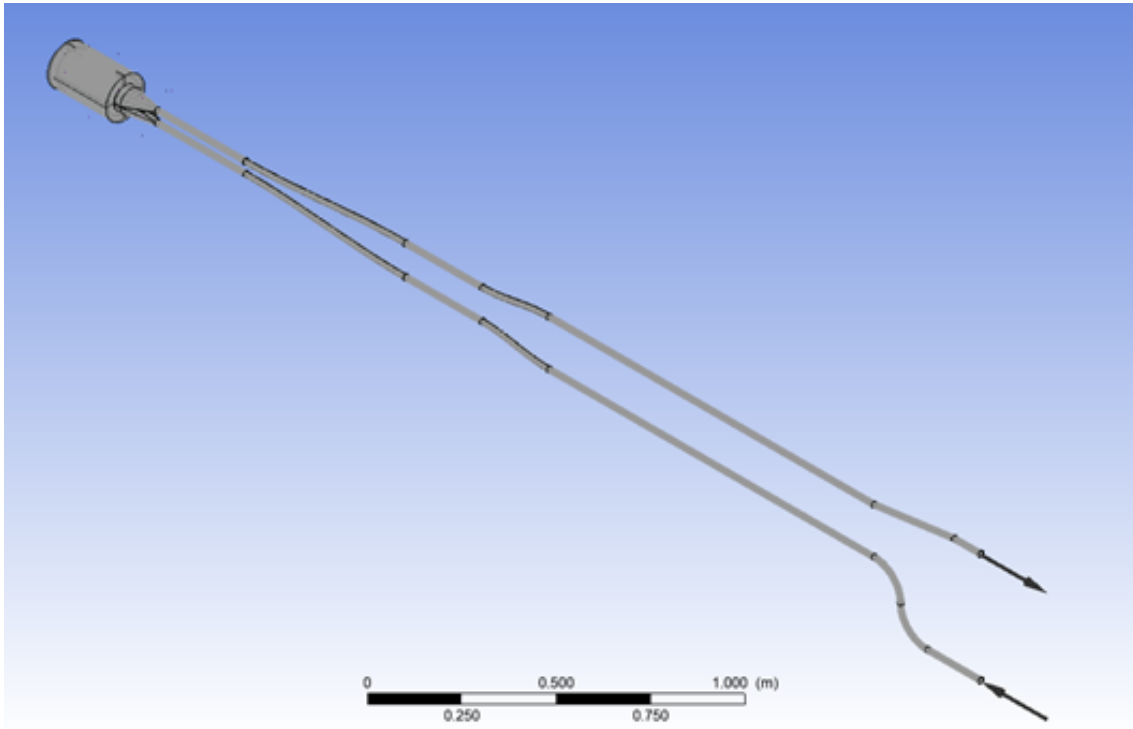


Figure 6.7: Inlet and outlet locations.

Table 6.2: Boundary Conditions

Location	Parameter	Value
Inlet	Mass flow rate	1 kg/s
Outlet	Static pressure	50 kPa
Interface, Domains	Wall	No slip wall
Fluid	Material	Water
Solid	Material	Aluminum
Fluid, Solid	Heat transfer	Isothermal

The fluid used is expected to be at standard temperature and pressure (STP) conditions and no significant temperature fluctuations are expected along the loop. The analysis is focused on the pressure and velocity behavior in the system. Hence, isothermal fluid with isothermal boundary conditions is assumed.

### 6.3.2 Flow model

In addition to boundary conditions, the selection of model is another part of the solution procedure. Steady-state model is used. The materials as defined in Table 6.2,

aluminum and water, are already included in the built-in ANSYS CFX database. Working fluid properties such as viscosity, density, and conductivity are provided within this database. The Shear Stress Transport turbulence model (SST) [16] is used for turbulence modelling with automatic wall function.

### 6.3.3 Solution procedure

This CFD analysis involves an iterative scheme. After a certain number of iterations, the solution must converge. A converged solution is reached when the residuals reach sufficiently low level. Residuals could be roughly defined as the mean difference between two consecutive solutions. This residual could be set in the SOLVER CONTROL as well as the number of maximum iterations. Generally, higher number of iterations and lower residual targets produce better convergence. Further, a monitor point for maximum  $^{16}\text{N}$  concentration  $N_{max}$  is set at the outlet to observe the stabilization of the system. Table 6.3 presents the basic settings used for this study.

Table 6.3: Details of SOLVER CONTROL.

Settings	Parameter	Value
Convergence control	Iterations	1000 to 20000
Convergence criteria	Residual target	1e-6
Interface, Domains	Wall	No slip wall

### 6.3.4 Post-processing

This step includes the use of CFD-POST to visualize the results from the computation. The results file is loaded to the software. A location plane is selected to show a cross section of the model. From here, contour lines for parameters such as pressure and velocity can be drawn. The graphical results are presented and discussed in Chapter 7.

# Chapter 7

## Inclusion of the transport equation for $^{16}\text{N}$

Another aspect included in this study is the production of  $^{16}\text{N}$  along the irradiation loop. To do this, a transport equation for  $^{16}\text{N}$  is included in the solver in the form of equation 2.2. There are multiple ways to let the ANSYS CFX interpret this equation, the bottom line is to have a production source (say, where the  $^{16}\text{N}$  formation is generated). It is also known that the produced  $^{16}\text{N}$  decays along the loop. From equation 2.2 we know that,

$$\frac{dN(t)}{dt} = R - \lambda N ,$$

The first term  $R$  presents the source and the second term  $-\lambda N$  is the decay term.

To insert the above equation in ANSYS CFX, the following options are considered:

- Option 1: Create two variables for the two terms and put them in the same subdomain (the fluid domain), defining necessary boundary conditions for both terms. Another variable shall then be created to combine the effects of both terms, with necessary expressions, so as to define the final concentrations value.
- Option 2: Create one additional variable, then create necessary expressions encompassing the first, second, and summation of equation 2.2.

For Option 1, we have the benefit of having only one expression but three different additional variables, each with its own boundary condition which could easily be confusing and redundant. For Option 2, although three expressions must be created, we only need one additional variable  $N$  which already represents the target concentration  $^{16}\text{N}$  that we want to analyze. By doing this, we only need to define one boundary condition at the inlet. Furthermore, it has the benefit of simplicity, wherein we could easily visualize the basic equation 2.2 in its physical form and as inserted in ANSYS CFX.

## 7.1 Loading the reaction rates

In defining the source term for the model, the reaction obtained from [2] have been used. Figure 7.1 presents the snail part of the model closest to the reactor core, with the corresponding raw data for reaction rate values [2][3]. These reaction rates inside the JSI TRIGA irradiation channels are calculated using the Monte Carlo neutral particle transport code (MCNP) program [17]. The reaction rates were calculated using the ENDF/B-VIII.0 [18] library as it is the most up-to-date nuclear data library and there are no significant differences in the cross-section between nuclear data libraries.

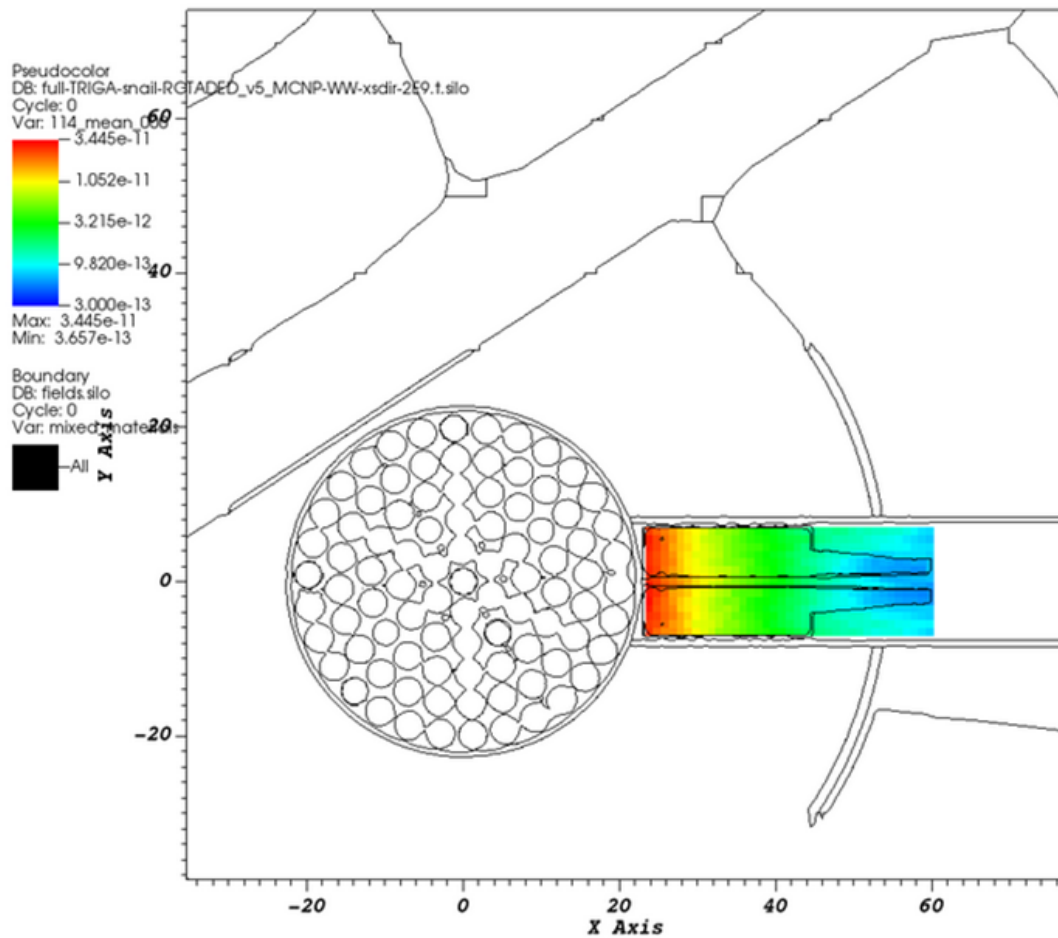


Figure 7.1: Reaction rate map for JSI TRIGA (in  $\text{cm}^{-3}\text{s}^{-1}$  [3]).

The raw data, presented in Figure 7.1 are interpreted as “the number of interactions taking place in one cubic centimeter per second” and are normalized to one source neutron. Although, against common interpretation, MCNP calculation is actually missing the average time spent in the volume of interest. The scaling factor  $C$  must therefore have units of  $\text{s}^{-1}$  [19].

As the focus of the study is water activation at full power, these reaction rates must be normalized. To do this, a scaling factor  $C$  is calculated using [19]:

$$C = \frac{P\nu}{Ek}, \quad (7.1)$$

where  $P$  is the reactor power,  $k$  is the calculated multiplication constant,  $\nu$  is the number of neutrons produced per fission and  $E$  is the average energy released per fission.

Equation 7.1 can be intuitively explained such that a reactor operating at  $P$  is powered by  $P/E$  fission events per second. This reactor produces  $P\nu/E$  fission neutrons per second. On the other hand, MCNP calculations of flux are normalized in such a way that the fission neutron production equals  $k$ . The scaling factor must therefore equal  $P\nu/Ek$  [19].

Table 7.1: MCNP reaction rate normalization terms.

Parameter	Value
reactor power, $P$ (J/s)	250 000
neutrons produced per fission, $\nu$	2.44
energy released per fission, $E$ (J)	3.17E-11
multiplication constant, $k$	1.05057

Table 7.1 presents the values for the given terms which are calculated using MCNP based on the core configuration as per an ongoing study [3]. From these values, a scaling factor  $C$  of  $1.83 \times 10^{16}$  is used to multiply the raw reaction rates. Figure 7.2 presents the normalized reaction rates values in  $m^{-3}s^{-1}$ .

## 7.2 Transport equation for a passive scalar

The passive scalar transport equation requires the definition of volumetric source and sink terms. The radioactive decay of passive scalar acts as a sink, and the generation of the scalar from activation near the reactor core acts as a source according to equation 7.2:

$$\frac{\partial(\rho\varphi)}{\partial t} + \nabla \cdot (\rho\mathbf{U}\varphi) = \nabla \cdot (\rho D_{\Phi} \nabla \varphi) + S_{\varphi}, \quad (7.2)$$

Rewriting to the form applicable to this case:

$$\frac{\partial(N)}{\partial t} + \nabla \cdot (uN) - \nabla \cdot (D\nabla N) = S_{activation} + S_{decay}, \quad (7.3)$$

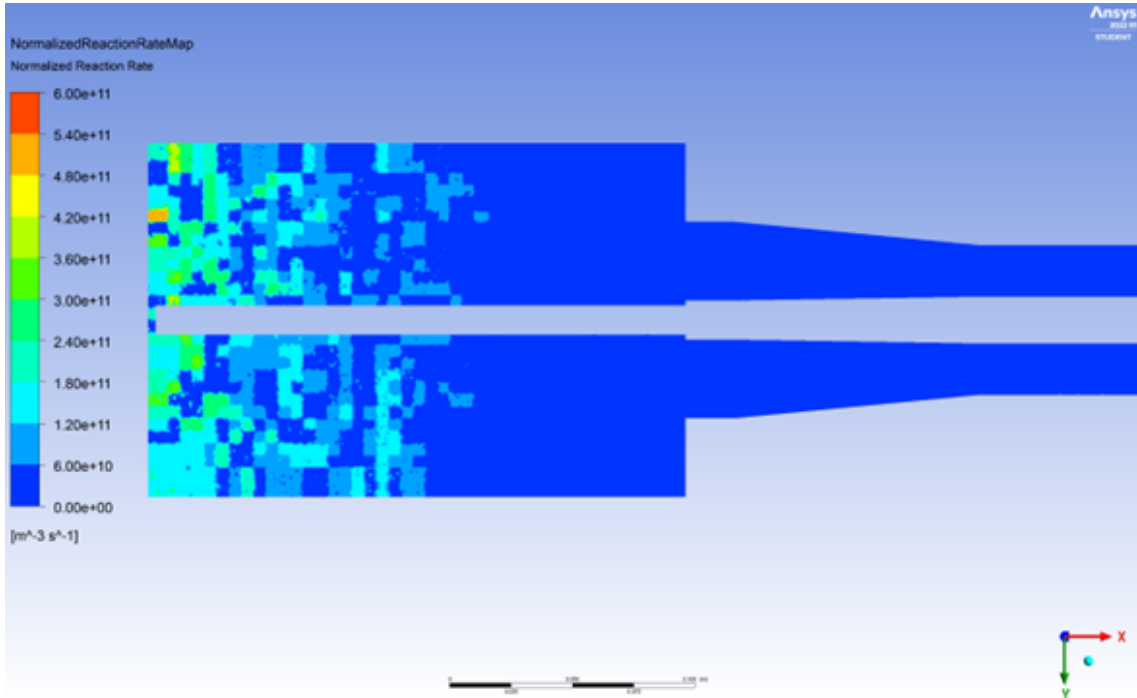


Figure 7.2: Normalized reaction rates  $[m^{-3}s^{-1}]$  for TRIGA reactor at full power of 250 kW.

where  $D$  is a diffusivity constant defined in later in Table 7.1 and  $S_{decay}$  and  $S_{activation}$  are the volumetric sink and source terms of  $N$ .

$$S_{decay} = -\lambda N, \quad (7.4)$$

$$S_{activation} = R, \quad (7.5)$$

An additional variable for concentration  $N$  is added with basic settings as defined on Table 7.2. The value of decay constant  $-\lambda$  is defined in the next chapter, in Table 7.3.

Table 7.2: Basic settings for additional variable  $N$ .

Settings	Parameter
Variable type	Volumetric [per unit volume]
Units	$molm^{-3}$
Tensor type	scalar



This variable is defined as a transport equation in ANSYS CFX to convect and diffuse  $^{16}\text{N}$ . Boundary conditions for  $N$  also has to be set at the inlet. The following stages are considered:

- Stage 1: Initial concentration at the inlet is zero.
- Stage 2: Inlet concentration for  $N$  is equal to the outlet concentration calculated from stage 1.
- Stage 3: Inlet concentration is the concentration  $N$  multiplied by a factor equal to the percent difference between the inlet and outlet of stage 2.

As discussed in the geometry section, the model used here represents only half of the full facility, which also includes the mirror loop connected to the outlet of the modelled loop. In stage 1, only the loop on the side of the reactor core is modelled. The source is present and the decay is solved according to equation 7.4. Fresh water is assumed; hence zero initial concentration is set at the inlet boundary.

For stage 2, we wanted to know the behavior of the  $^{16}\text{N}$  concentration once it exits the loop near the reactor core and goes through the mirror loop. This mirror loop has no source and hence only the decay of  $^{16}\text{N}$ , following the Eq. 7.3 is considered. The outlet concentration calculated from stage 1 is set as the inlet concentration for stage 2  $N_2^i$ .

From the results of stage 2, an outlet concentration  $N_o^m$  from the mirror loop is defined. A multiplier is calculated wherein

$$multiplier = 1 - \left( \frac{N_2^i - N_o^m}{N_2^i} \right), \quad (7.6)$$

This factor multiplied by the outlet concentration variable of stage 3 is set as the inlet concentration boundary condition for stage 3. In this way, a full picture of the irradiation facility could be considered.

### 7.2.1 ANSYS CFX expressions for additional terms

Expressions for additional terms are defined according to equations 7.4 and 7.5 and making sure that corresponding units are followed.

$$Activation = (1/avogadro) * Subdomain1.R(x, y, z), \quad (7.7)$$

$$Decay = -0.0972[s^{-1}] * N, \quad (7.8)$$

$$N_{source} = Activation + Decay, \quad (7.9)$$

Note that for stage 2 where only decay is studied, equation 7.7 is not present. Finally, a subdomain is created to define the source term. For this case, it consists only of the fluid domain. Equation 7.9 is inserted herein. Table 7.3 presents the constants used in defining the additional variable.

Table 7.3: Constants for additional variable [5][6]

Parameter	Value
Decay constant, $\lambda$	$0.0972 \text{ s}^{-1}$
Diffusivity constant for nitrogen in water, D	$1.9\text{E-}9 \text{ m}^2/\text{s}$

# Chapter 8

## Results and discussion

The pressure and velocity parameters were analyzed based on the results of the simulations. The results for the additional variable of  $^{16}\text{N}$  were also presented. The parameters examined are summarized on Table 8.1.

Table 8.1: Summary of steady-state simulation results.

Parameter	Value
Pressure drop	73960 Pa
Velocity	Max: 5.5 m/s
$^{16}\text{N}$ concentration [ $m^{-3}$ ]	Inlet average: 1.56E11 Outlet average: 2.38E11 Max: 2.95E11 Min: 1.5E11

A pressure drop of around 74 kPa with a maximum velocity of 5.5 meters per second was calculated.  $^{16}\text{N}$  outlet concentration average of  $2.38 \times 10^{11}$  particles per cubic meter were calculated. Further analysis of the behavior of the parameters in the model is discussed in the succeeding sections.

Figures 8.1 and 8.2 present the pressure profile in the model for a steady-state simulation. Pressure decreases from the inlet as the fluid flows downstream to the outlet.

From Figure 8.1, a proportional and constant change in pressure could be observed. After overcoming the constrictions of a smaller pipe upstream and the fluid reaching the snail portion of the model, decrease in pressure is observed. Further, looking at the profile from Figure 8.1 (bottom), it could be seen that the pressure distribution along pipe cross-section is constant.

Figure 8.2 provides a closer look of the pressure profile along the snail where more disturbances in the flow could be expected because of the fluid turns and change in directions owing to the structure of the snail. After traversing upstream

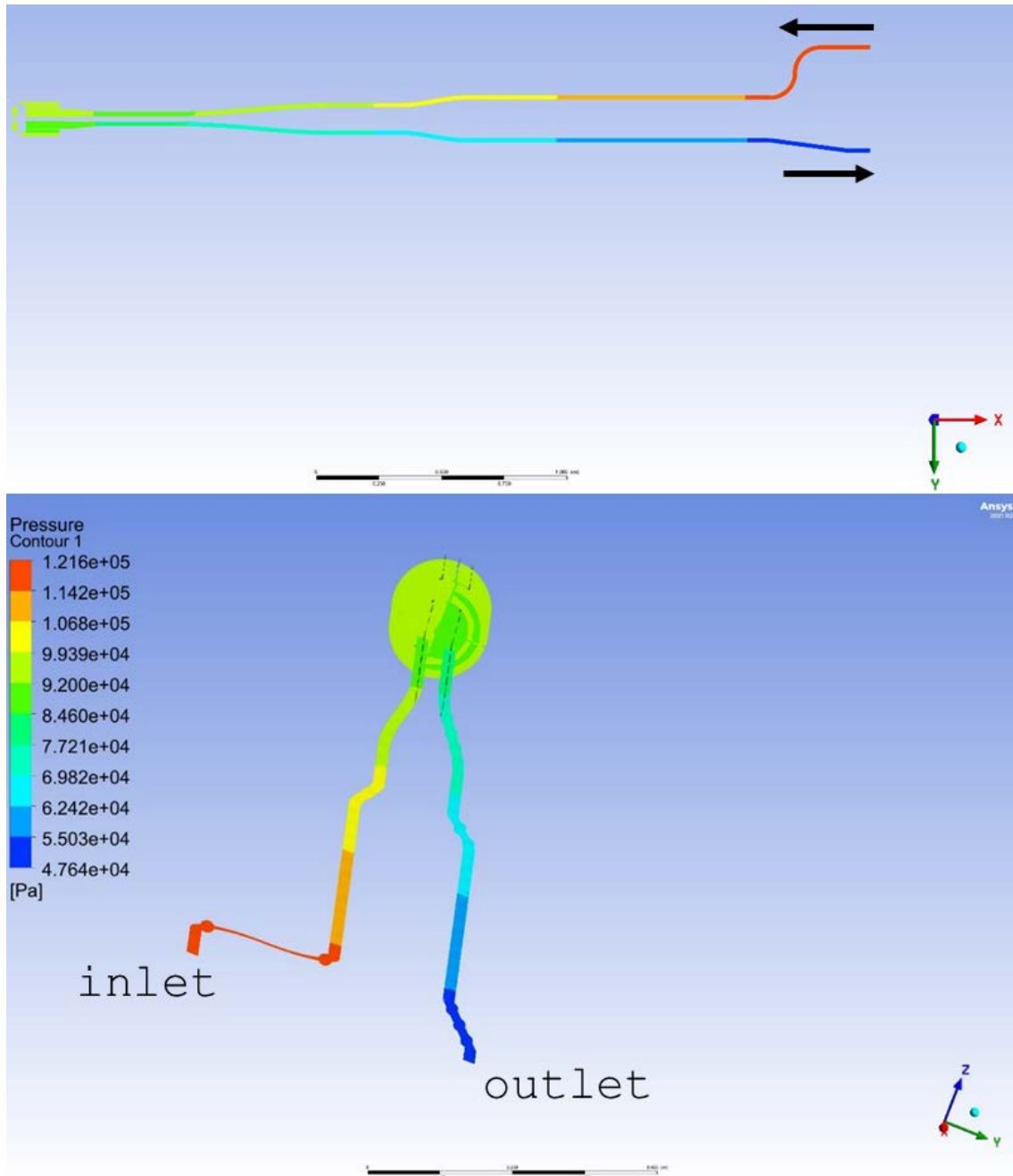


Figure 8.1: Pressure profile results.

from the inlet pipe, the fluid makes a total of three turns on the first half of the snail before reaching the other half and subsequently downstream to the outlet pipe.

Stable pressure could be noted on the first half of the snail and remains the same until the fluid enters the second half on its first turn. After entering the second turn, the pressure then decreases. It remains constant until it exits the snail and enters downstream to the outlet.

It could be expected that pressure increase on the snail exit constriction would take place, however, as the overall velocity has already decreased due to comparably large

---

area of the snail, the effect balances out.

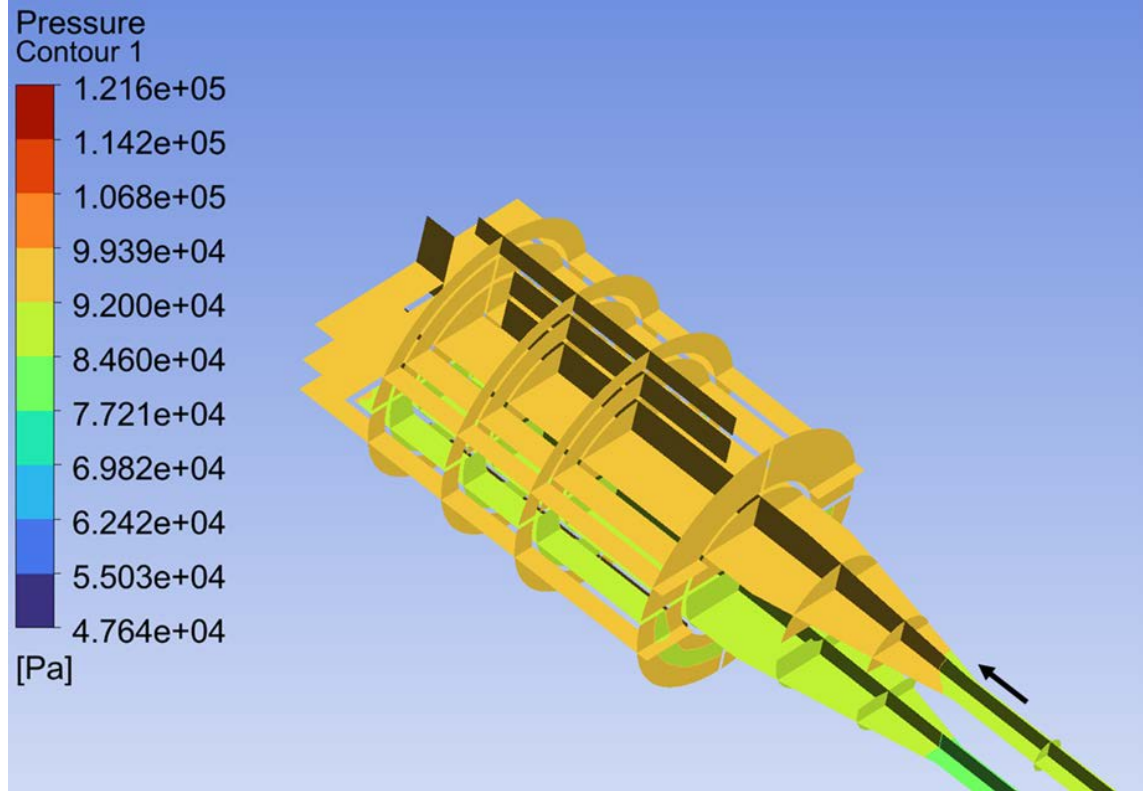


Figure 8.2: Pressure profile results in the snail part.

Figures 8.3 to 8.5 presents the velocity profile in the model in a steady-state simulation. Maximum velocity is registered along the upstream and downstream pipes of the inlet and outlet pipes, respectively.

From Figure 8.3, it could be seen that higher velocities are recorded along the upstream and downstream pipes. This is expected owing to the smaller cross-section of these pipes compared to the snail. Hence, it is also observed that lower or zero velocities are recorded in the snail part.

Figures 8.4 presents a closer look of the fluid flow upstream and downstream. The inlet upstream velocity profile shows a constant variation of the velocity along the pipe cross-section, which could be attributed to the presence of wall boundary. Moreover, it could be observed that velocity increase took place earlier in the middle part of the pipe cross-section. A more noticeable velocity decrease is observed at the bend of the inlet pipe owing to the friction and sudden change in flow direction it causes.

The downstream pipe to the outlet shows a more stable velocity as no unexpected pipe bends are present herein. A more detailed look on the velocity profile on the snail portion is presented on Figure 8.5.

As the fluid approaches the entrance part of the snail, huge and apparent decrease

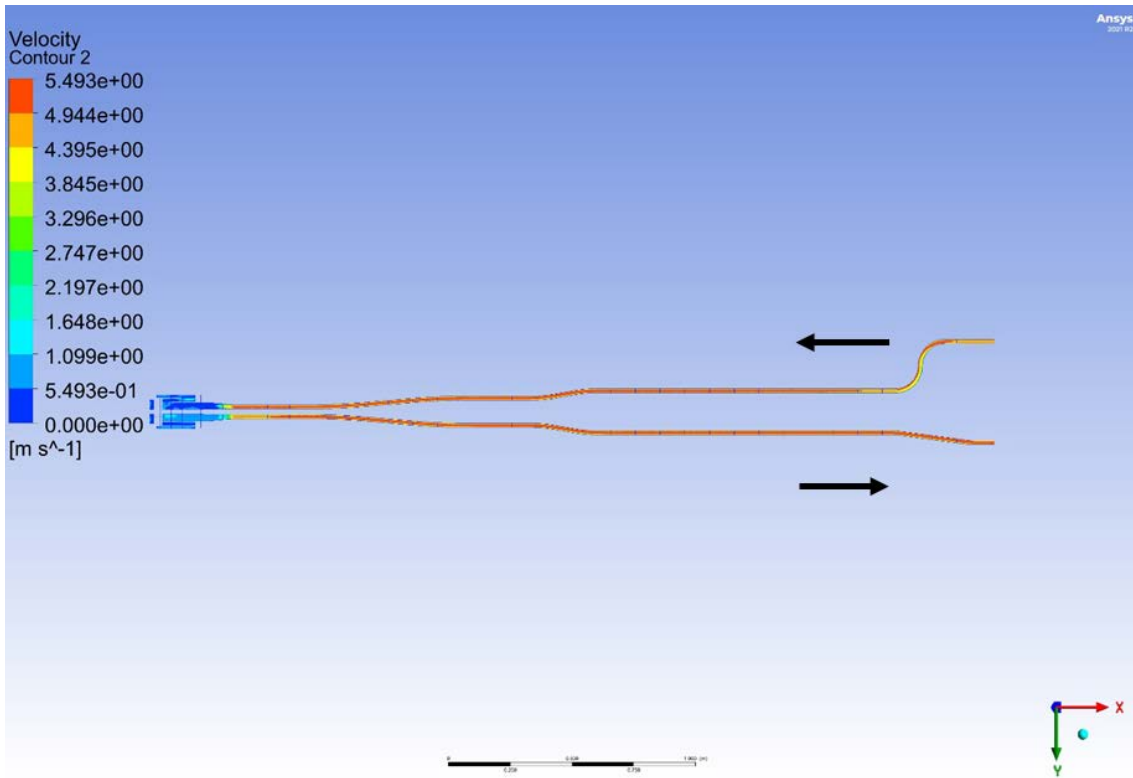


Figure 8.3: Velocity distribution.

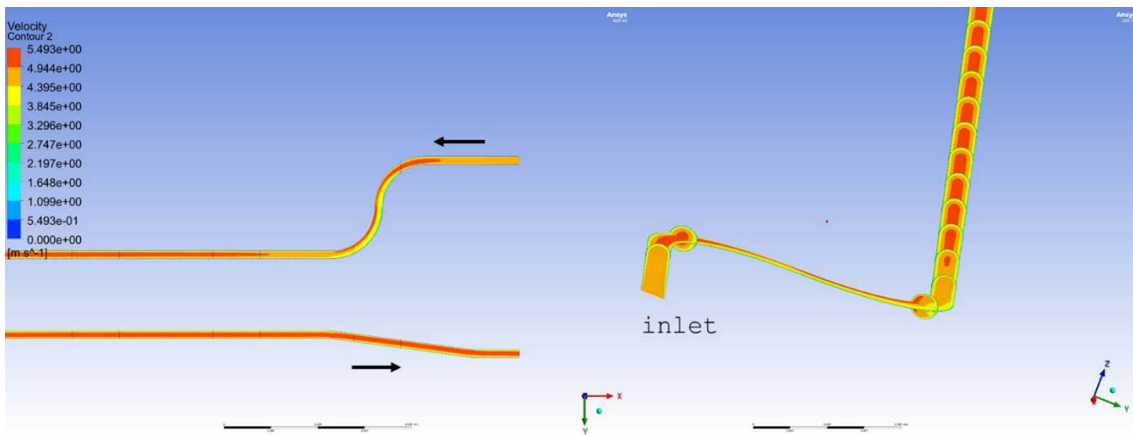


Figure 8.4: Velocity profile results at inlet and outlet boundaries.

in velocity is observed. Note that a very slight increase in pressure with the same behavior is observed in the same location (as in Figure 8.2). This velocity decrease is expected as the area of the snail is significantly larger than the that of the pipe.

Moreover, significant changes in velocity are also observed as the fluid fully enters the snail. The presence of the wall boundary also contributes to this behavior. Thus, as the fluid enters the snail, the flow is significantly slowed down. The presence of the structures made to redirect the fluid seem to aid the motion. However, it could be observed that although sharp velocity increase took place at this baffle bound-

aries, flow seem to die down quicker too as the fluid tries to stabilize itself.

## 8.1 $^{16}\text{N}$ concentration

Table 7.3 shows the boundary conditions set and calculated at each stage of additional variable  $^{16}\text{N}$  calculation. The results of the simulations based on these boundary conditions are presented on Figures 8.6 to 8.15.

Table 8.2: Boundary conditions for additional variable  $N$ .

Parameter	Value
Stage 1 outlet/ stage 2 inlet, $N_2^i$	1.35E11 [ $m^{-3}$ ]
Stage 2 outlet, $N_o^m$	8.88E10 [ $m^{-3}$ ]
multiplier	0.657

On stage 1, fresh fluid entering is used, and no trace of  $^{16}\text{N}$  is assumed. The outlet  $^{16}\text{N}$  concentration value computed from this simulation is used as inlet feed to stage 2 where  $^{16}\text{N}$  decay is modelled and there is no presence of the source. This is conducted to reproduce the behavior in the mirror loop connected to the modelled loop near the reactor core discussed herein. Finally, a full picture of the whole irradiation loop is modelled in stage 3, wherein the concentration computed from the  $^{16}\text{N}$  decay on stage 2 is used as the inlet instead. The concentration profile results for stage 1 (fresh fluid feed) are presented on Figures 8.6 to 8.8.

Figure 8.6 presents the  $^{16}\text{N}$  concentration summary for fresh fluid entering the inlet. It could be seen that  $^{16}\text{N}$  production is only observed when the fluid reaches the entrance of the snail part.

As the fluid is exposed to activation, an increase in  $^{16}\text{N}$  concentration can be observed. This is more pronounced on the second half of the snail. Although both parts of the snail are exposed to the same amount of neutron flux, the fluid in the second part has spent a longer residence time in the snail. Hence, the increased exposure time contributed to the increased  $^{16}\text{N}$  concentration in this area. Further, as the fluid exits the second half of the snail and flows downstream, it farther decays midway to the outlet.

The fluid entering and exiting the snail is shown in more detail on Figure 8.7. The contour shades are labelled (i.e. 1,2,3, etc.) and marked in the figure, and are referred in succeeding texts for easier interpretation. Once the fluid breaches the entrance to the snail, subsequent increase in  $^{16}\text{N}$  concentration is observed (Figure 8.7 – middle 2, 3). The concentration continues to increase (Figure 8.7 – middle 8)

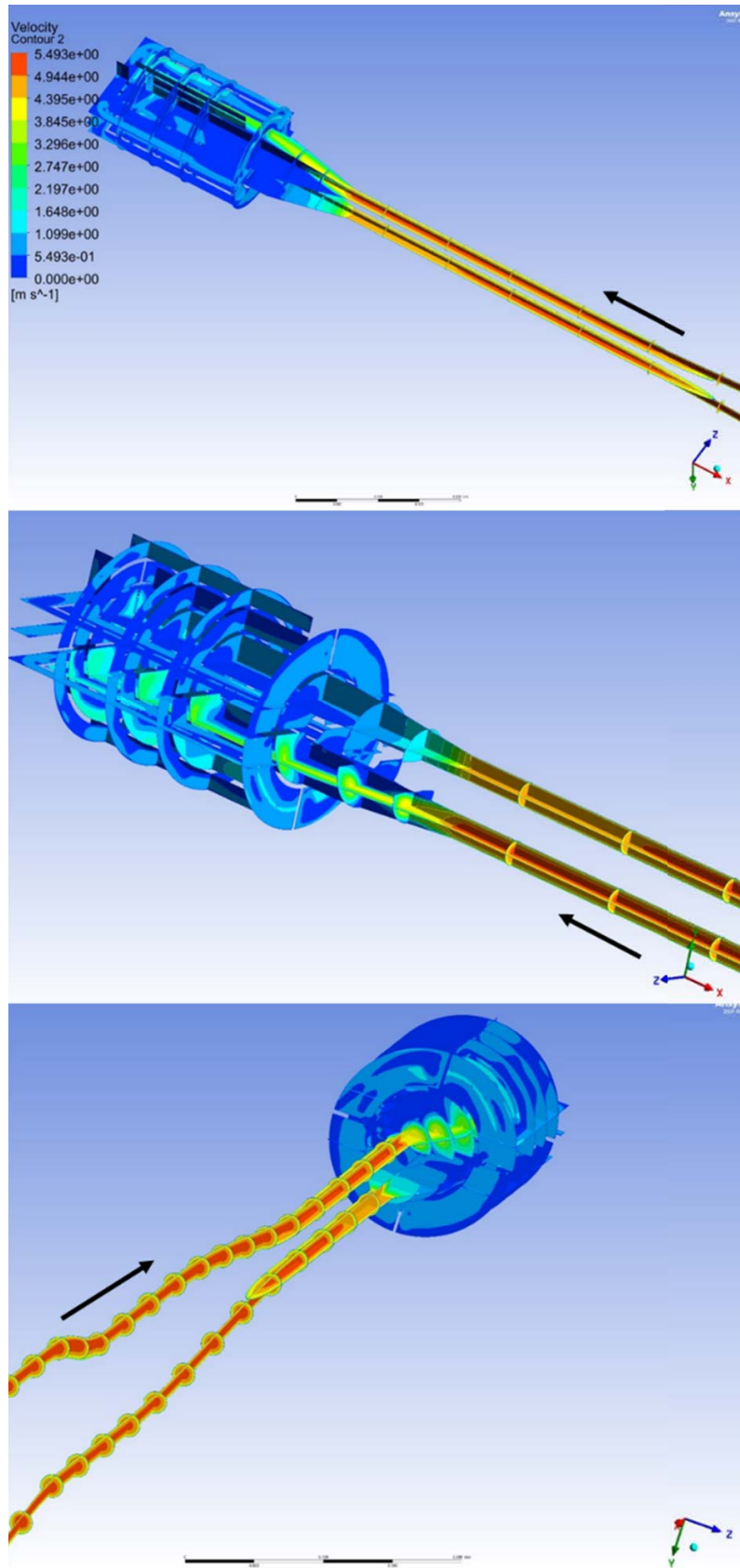


Figure 8.5: Velocity profile results at various viewing angle.



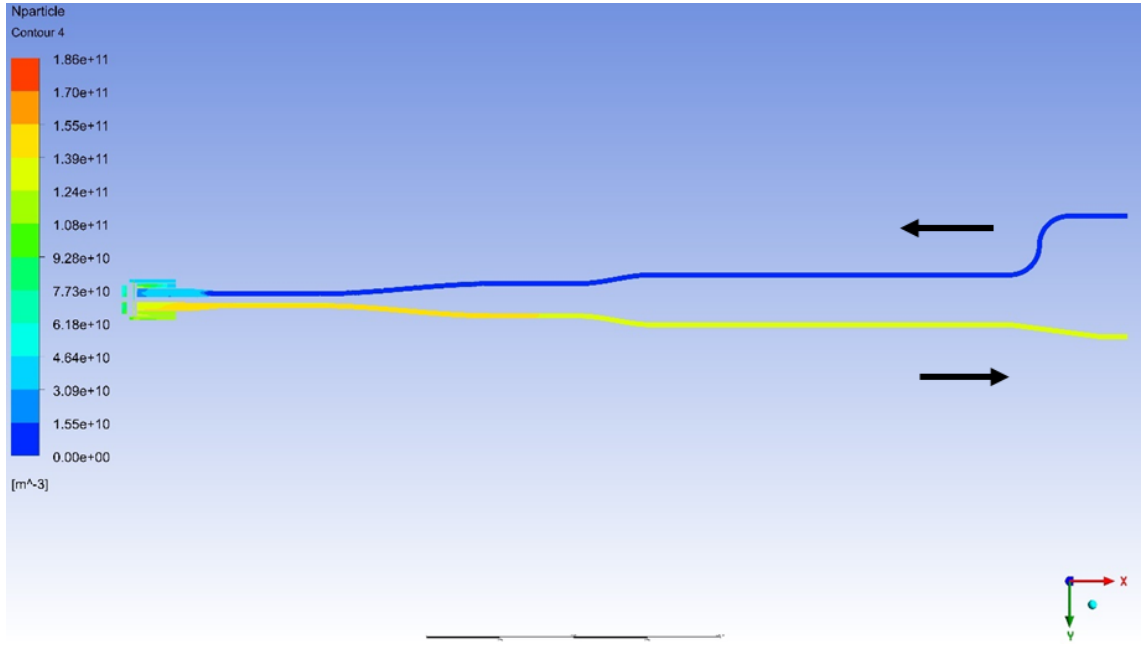


Figure 8.6:  $^{16}\text{N}$  concentration profile results from stage 1.

at the fluid's last turn in the first half portion of the snail.

Maximum concentration is observed at points (Figure 8.7 – middle 12, 13) where the fluid reaches its final turn in the second half of the snail, on its way to exit downstream. Furthermore, although quite high concentrations (Figure 8.7 – contour 11, 12) are observed at the snail exit, some decays (contour 10) could be noted beside it, close to the baffle boundary. This could be attributed to comparably higher velocity near the same area (as seen on Figure 8.5) compared to the surrounding fluid. This higher velocity could be attributed to the existing structures within the snail. Notice that the referred low  $^{16}\text{N}$  concentration is located above the portion between the second and third turns on the downstream (second half) of the snail. While the flow below it takes time to recover from the impact of sudden turns, above it has more area, and hence higher velocity since it has more room for flow. This could lead to fluid being replaced faster, hence, lesser of the  $^{16}\text{N}$  particles detected. On the other hand, downstream of this area, higher concentrations are then observed.

The location of the maximum  $^{16}\text{N}$  concentration at (Figure 8.7 – middle 12, 13) could also be explained by this phenomenon. Aside from the fact that this is located at the last turn and amongst the longest residence time in the snail, the choke point between the second and third turns (downstream second half of the snail) makes the fluid flow slower, therefore the residence time is longer, subsequently leading to higher exposure time. This is more evident from Figure 8.8, wherein almost the whole portion of the fluid in contact with the wall for the last turn has higher concentration than the others.

The concentration profile results for stage 2 (decay of  $^{16}\text{N}$ ) are presented on Figures 8.9 to 8.11. Figure 8.9 presents the  $^{16}\text{N}$  concentration summary for the decay of  $^{16}\text{N}$ .

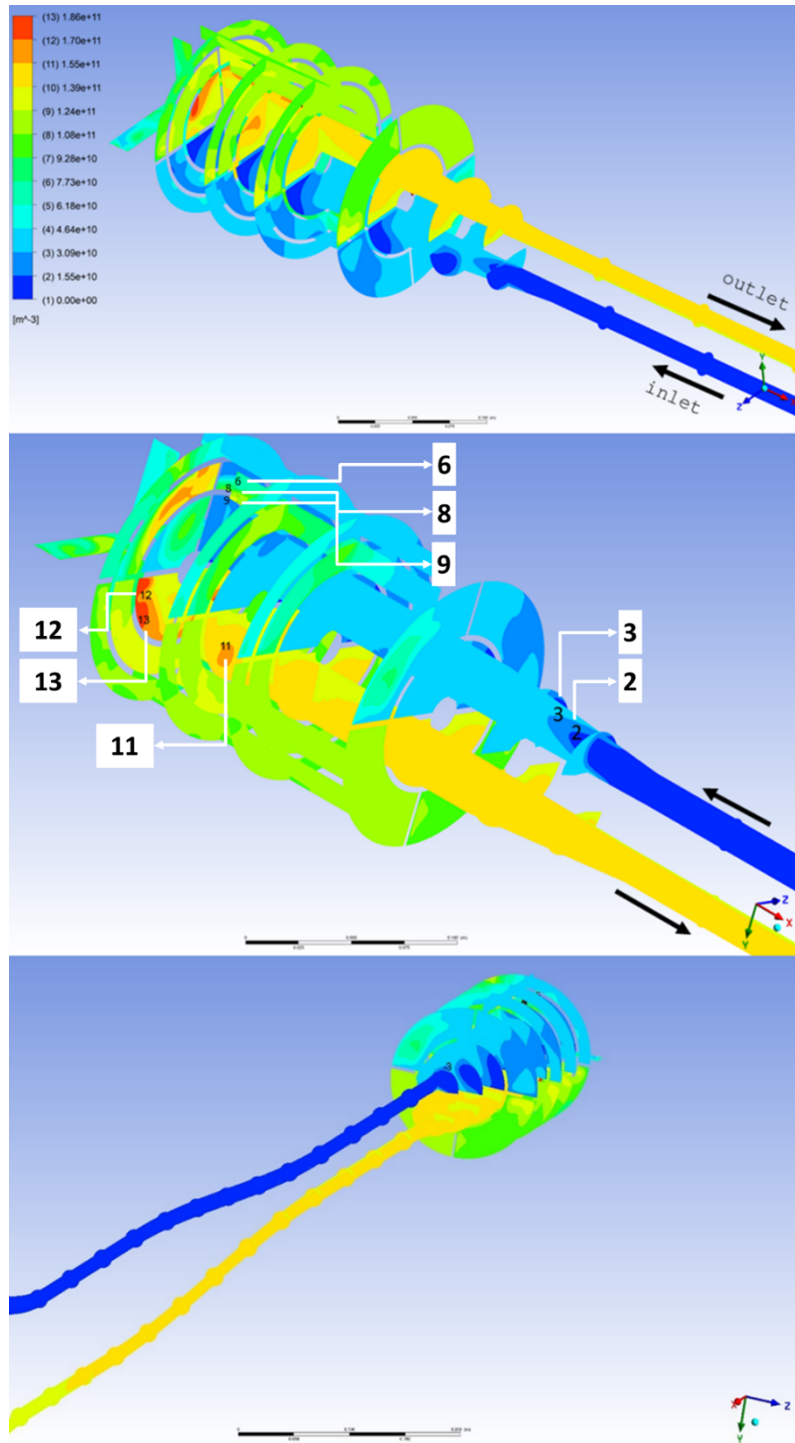


Figure 8.7:  $^{16}\text{N}$  concentration profile results at snail from stage 1.

From this, it could be estimated that around thirty-five percent of  $^{16}\text{N}$  concentration is decayed along the mirror loop.

Along the inlet and outlet pipe, the decay is constant. As the fluid approaches the snail entrance, a more erratic decay is observed. As velocity and pressure changes vary as does the structure of the snail, residence time also differs. It could be observed from Figure 8.10 that such behavior indeed affects the  $^{16}\text{N}$  decay.

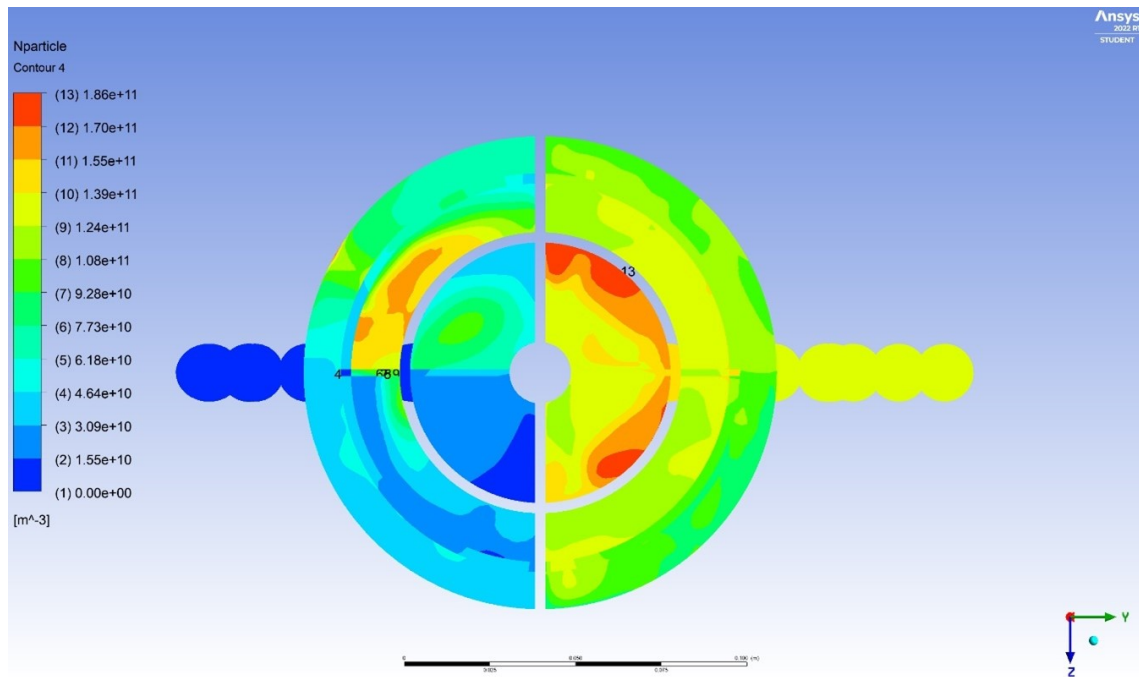


Figure 8.8:  $^{16}\text{N}$  concentration profile results from stage 1, view adjacent to reactor core.

It is mentioned that the fluid does not enter the snail at uniform velocity due to presence of internal structures and wall boundaries. This is evident in Figure 8.11, where the erratic fluid velocity entering the snail affected the first turn at snail upstream (first half of the snail).

Higher concentrations are observed closer to the internal structure. This persists until the fluid exits the snail, wherein at the equivalent location, higher concentration is attained than in other parts of the fluid. Since no significant turbulence occurred in the snail even with the presence of sharp turns, fluid mixing is unlikely, therefore the location of the higher concentration remained predictable.

The concentration profile distributions for stage 3 are presented in Figures 8.12 to 8.15. Figure 8.12 presents the  $^{16}\text{N}$  concentration summary for stage 3 wherein the fluid exiting stage 2 is assumed to enter the model. This gives an overall view of the whole irradiation loop with the model adjacent to the reactor and the same model connected to its inlet and outlet pipes.

Overall, the same behavior as at previous stages seem to persist in the upstream pipe. Meanwhile, downstream, the concentration does not stabilize right away after exiting the snail, a behavior not observed in stage 1 with fresh fluid, but it is present at stage 2 without a source where only decay dominates. However, while in stage 2, this happens at the pipe bend within one meter, in stage 3 it takes place earlier just a few centimeters downstream from the snail exit.

The fluid entering and exiting the snail is shown in more detail on Figures 8.13 to

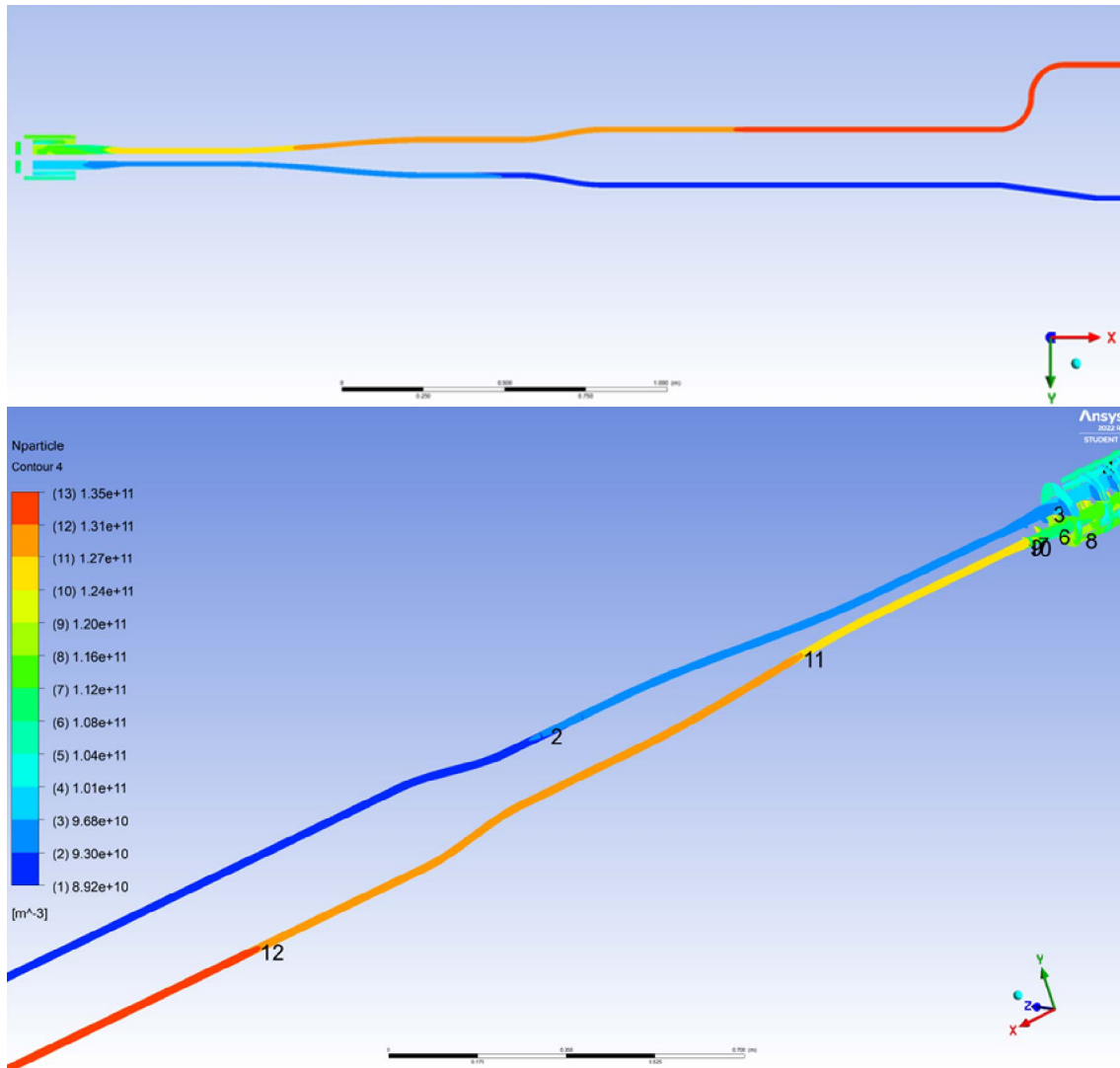


Figure 8.9:  $^{16}\text{N}$  concentration profile results from stage 2 (decay on mirror loop).

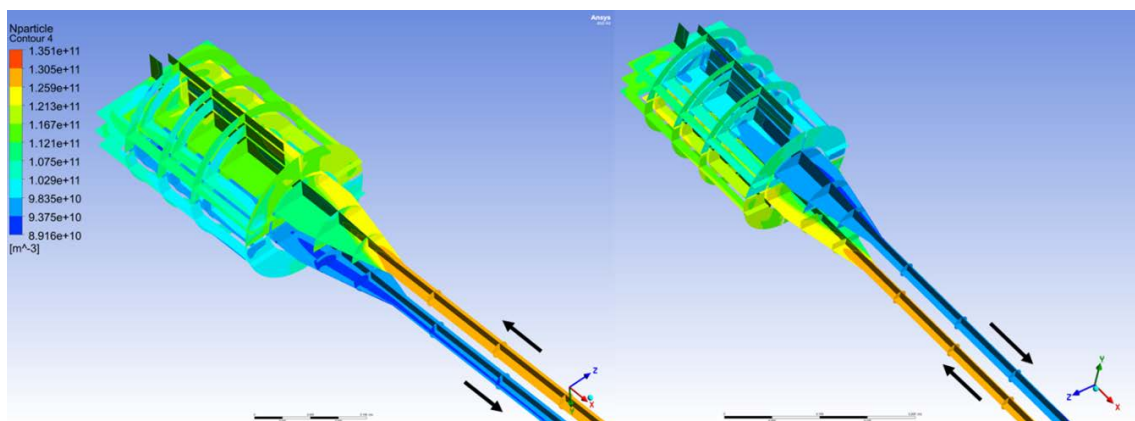


Figure 8.10:  $^{16}\text{N}$  concentration profile results at snail from stage 2 (decay on mirror loop).

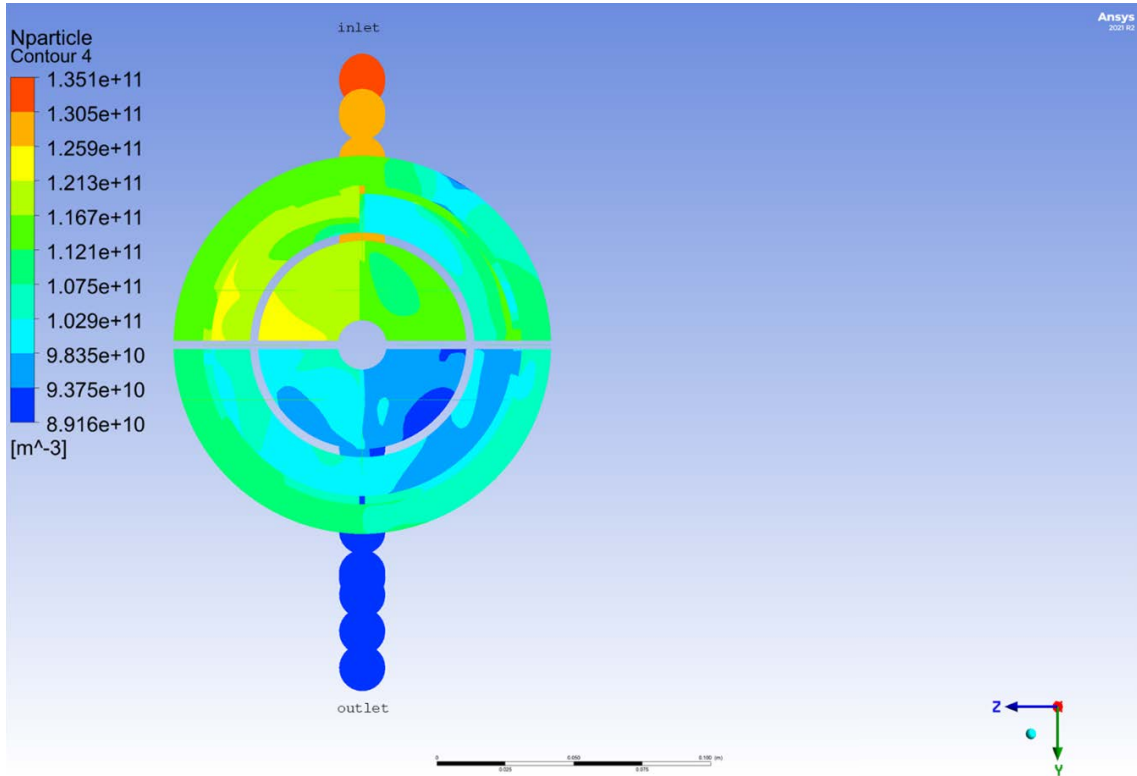


Figure 8.11:  $^{16}\text{N}$  concentration profile results from stage 2 (decay on mirror loop), view adjacent to reactor core.

8.15. As in previous stages, the behavior at the snail inlet and exit is the same. Also note the concentration variation (Figure 8.13 – top 5, 6, 8) just at the first turn on Figure 8.13. As discussed previously, the presence of structures causes some turbulence and subsequently difference on velocities and residence and exposure times. With the presence of bend as a choke point, higher concentrations are observed here and decreases as one moves farther from it.

While previously there is no such great concentration differences at these turns, it is more evident now and takes more time to stabilize. This could be attributed to the higher concentrations in the model compared to previous stages, as now it is assumed that activated fluid re-enters the model and is being activated repeatedly.

As in Figures 8.14 and 8.15, similar behaviors as in previous stages are observed. The location of the maximum concentration (Figure 8.14 – 12, 13) is also marked and may have occurred for the same reasons as in stages 1 and 2. Overall, the water activation loop is computed to have a maximum  $^{16}\text{N}$  concentration of  $2.95 \times 10^{11} \text{ m}^{-3}$  and an average of  $2.38 \times 10^{11} \text{ m}^{-3}$  at the outlet.

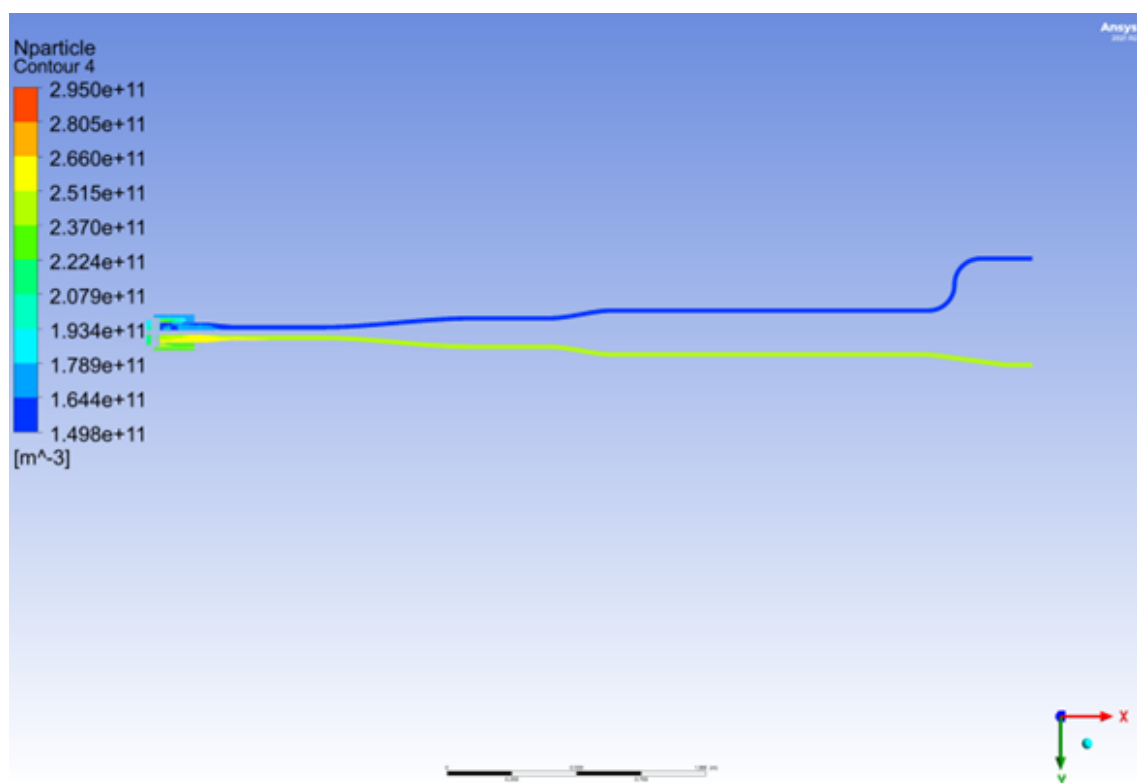


Figure 8.12:  $^{16}\text{N}$  concentration profile results from stage 3.

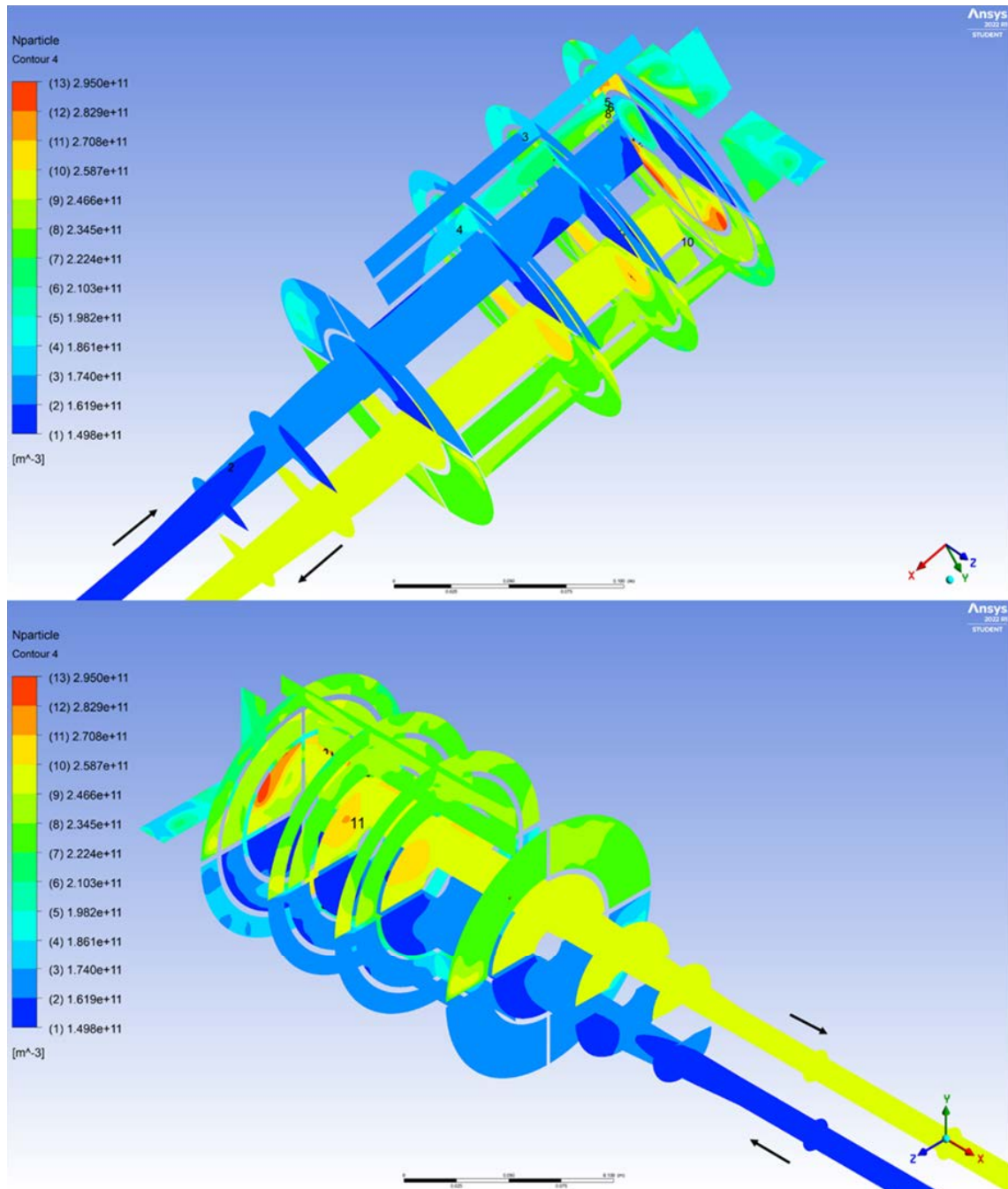


Figure 8.13:  $^{16}\text{N}$  concentration profile results at snail from stage 3.



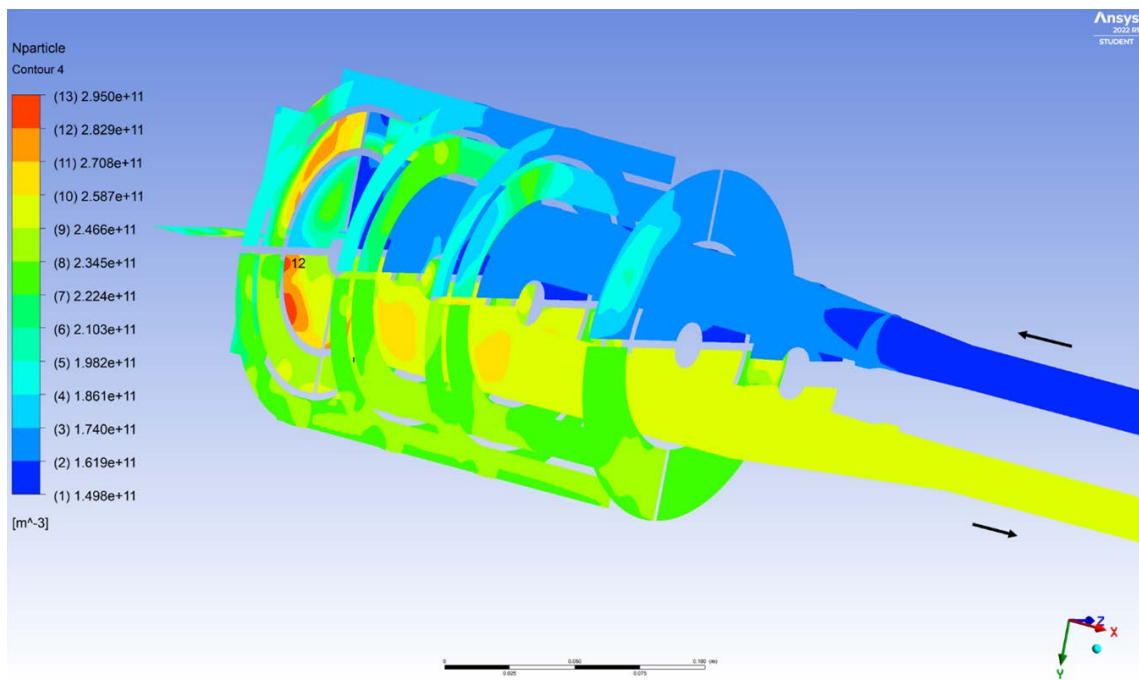


Figure 8.14:  $^{16}\text{N}$  concentration profile results at snail from stage 3. Side view.

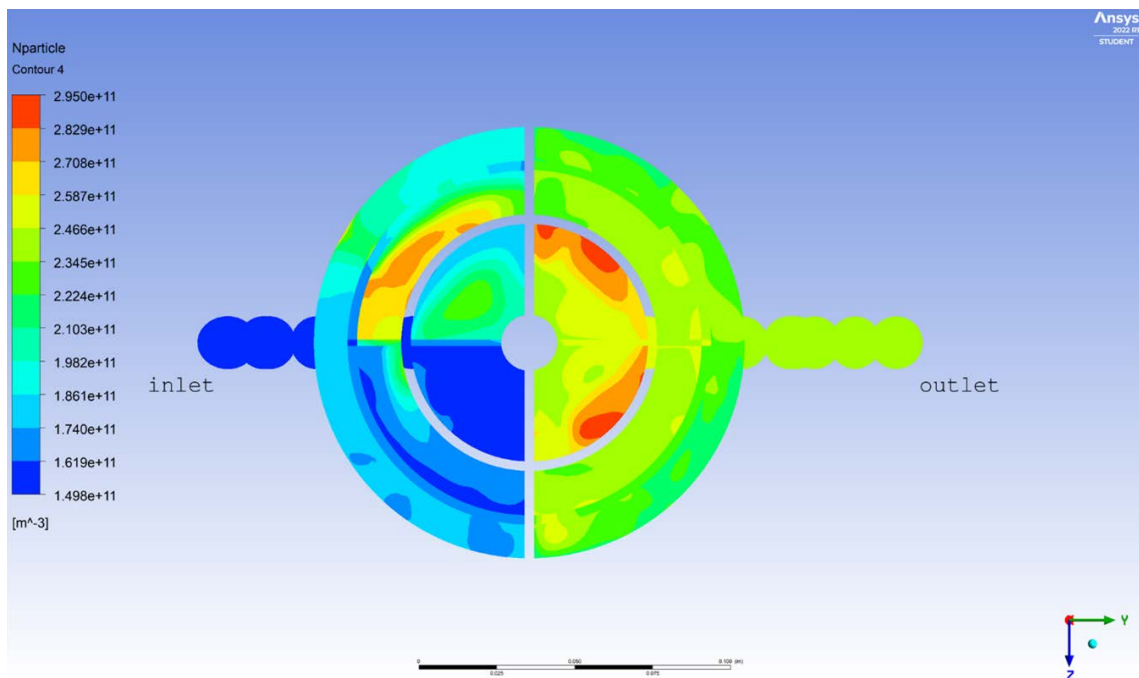


Figure 8.15:  $^{16}\text{N}$  concentration profile results from stage 3, view adjacent to reactor core.



# Chapter 9

## Verification

Simple verification is conducted to assess the feasibility and accuracy of the computed results. This verification includes the assessment of the residuals and imbalances [20], as well as comparison of ANSYS CFX simulation results with FLUENT simulations in terms of some relevant parameters. The accuracy of the additional variable simulation is also cross-checked by comparison with analytical results of decay equation.

### 9.1 Residuals and imbalances

Simulations with up to twenty-thousand iterations were performed for the model. The convergence of results was assessed using the residual and monitor plots as presented in Appendix C. Residuals ranging from  $10^{-4}$  to  $10^{-6}$  were observed at only a thousand iterations and remained constant even with twenty-thousand iterations. The imbalances were also monitored, except for the additional variable, this remained below  $10^{-4}$  throughout the simulations.

### 9.2 Additional variable imbalance

Even at a thousand iterations, it is observed that the results converge well already. However, this is not the case for the additional variable. As such, up to twenty-thousand iterations were performed to stabilize this variable. Appendix C presents the values registered for  $Nmax$ , which is the maximum value of additional variable  $^{16}\text{N}$  calculated during the iterations.

Figure 9.1 presents the  $Nmax$  data at twenty-thousand iterations. It could be observed that these  $Nmax$  seem to be very erratic and just keeps increasing as the computation continues. Looking at the plot of  $Nmax$ , it seems to stabilize after three-thousand iterations. Although this is not apparent unless more iterations are taken, then one could judge that its value fluctuates between a set data points.

Another factor considered is the N-fluid domain imbalances as presented on Appendix C and D. Table 9.1 summarizes the N-fluid domain imbalances for the sim-

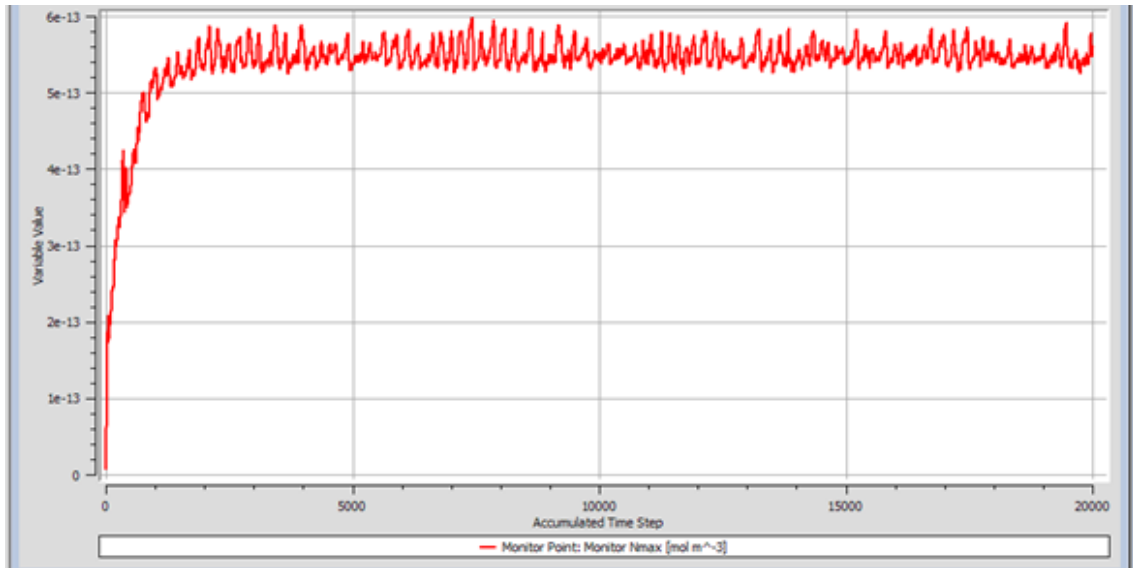


Figure 9.1:  $N_{max}$  plot for simulation at 20000 iterations.

ulations at specific iterations.

Table 9.1: Additional variable imbalance.

Number of Iterations	% Imbalance
1000	10.1231
3000	0.1372
5000	-0.0157
8000	-0.0051
10000	-0.0035
13000	- 0.0149
15000	0.0259
20000	0.0160

From Table 9.1, it could be seen that at five-thousand iterations, the imbalances significantly decrease and are later closer to zero. Ideally, an imbalance value close to zero is desired. Hence, even the results at five-thousand iterations is acceptable. For this study, the results at twenty-thousand iterations are presented as it could be observed that  $N_{max}$  stabilized further, more iterations are preferred as they allow to generate more data for the simulation results.

## 9.3 Comparison with the FLUENT results

A quick simulation with FLUENT has been performed excluding the additional variable. All initial parameters are similar and SST model is also utilized. Table 9.2 presents a comparison for the parameters calculated with FLUENT and ANSYS CFX. The pressure and velocity profile results from FLUENT are also presented on Figures 9.2 to 9.5.

Table 9.2: Results for irradiation loop simulation with FLUENT vs ANSYS CFX.

Parameter	FLUENT	ANSYS CFX
Pressure drop	80630 Pa	73960 Pa
Maximum velocity	5.7 m/s	5.5 m/s

From the values presented on Table 9.2, it could be seen that the calculated pressure drop, and maximum velocity are almost similar for both simulations. Small variations may be due to the inherent differences in the way each program performs its calculation. It should be noted that FLUENT simulations were conducted only as a “rough” check on the reliability of the ANSYS CFX results. A more thorough analysis is beyond the scope of this thesis.

Figure 9.2 presents the pressure distributions for FLUENT and ANSYS CFX. Though a quick look reveals that the decrease in pressure took place quicker downstream of the outlet pipe for FLUENT compared to ANSYS CFX which appears almost symmetrical to its upstream counterpart, it could be observed that there are no significant differences in the pressure distributions between the two calculations.

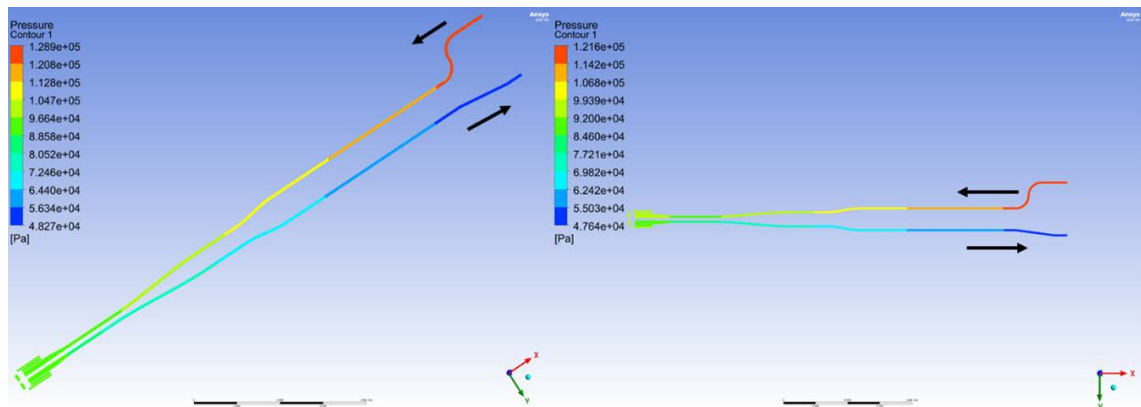


Figure 9.2: Pressure distribution results from FLUENT (left) and ANSYS CFX (right).

Figure 9.3 presents the velocity results for FLUENT and ANSYS CFX. Similar as for the pressure profile, the velocity behavior is almost identical for both FLUENT

and ANSYS CFX. Although, there are minute differences in the values, but this is expected as mentioned earlier.

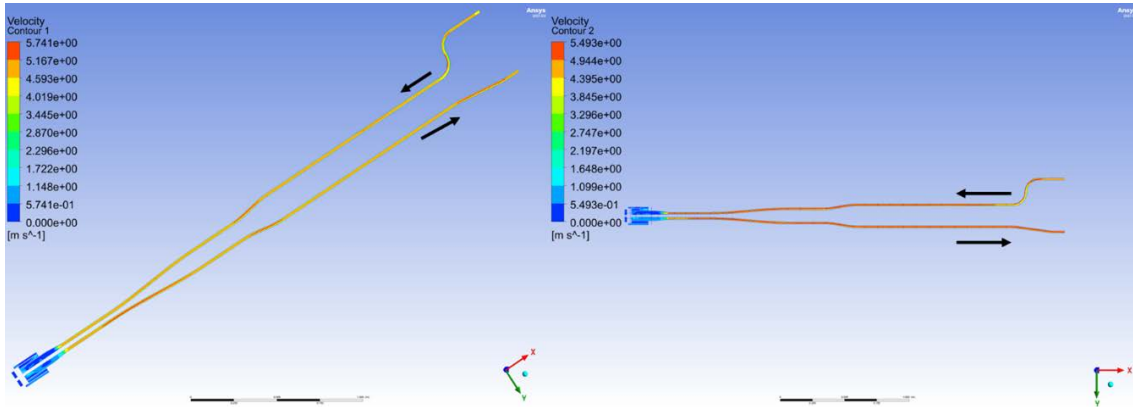


Figure 9.3: Comparison of velocity distributions between FLUENT (left) and ANSYS CFX (right).

Figure 9.4 presents a closer look of the snail portion of the velocity profile for FLUENT and ANSYS CFX. Generally, the behavior is the same in terms of overall decrease in velocity as fluid enters the snail. Minute increase in velocity is also observed as the fluid reaches the turns in the snail internal structure. Small variations in terms of localized changes in velocity is observed, particularly on the last turn on the second half of the snail leading to exit downstream. Instead of a uniform snail exit velocity as in ANSYS CFX, localized decrease in velocity is registered for FLUENT.

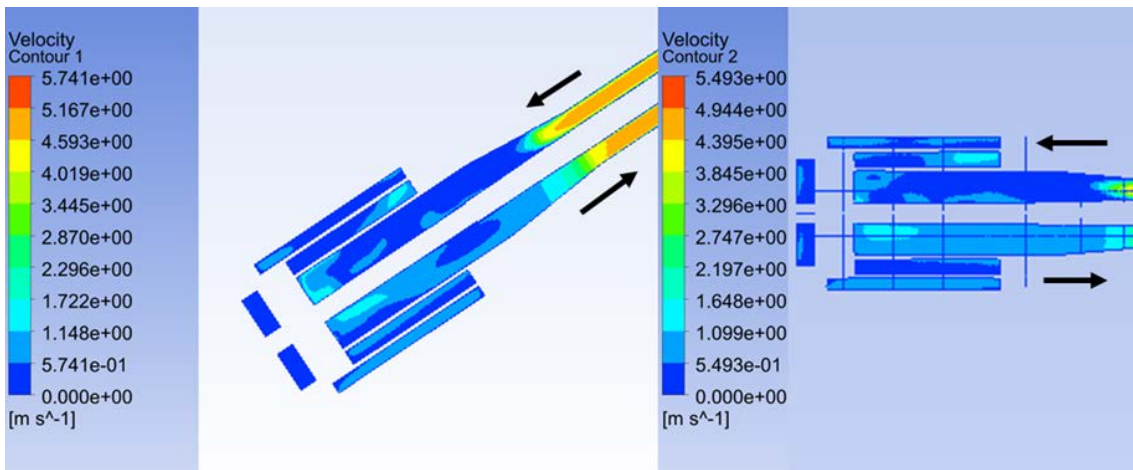


Figure 9.4: Velocity profile results in the snail part from FLUENT (left) vs ANSYS CFX (right).

Figure 9.5 presents a closer look of the velocity profile at the inlet and outlet section of the model for FLUENT and ANSYS CFX. Again, the fluid behavior is generally the same in terms of expected overall increase and decrease in velocity; except for

small, localized velocity variations that is present on FLUENT profile results compared to a uniform profile as with ANSYS CFX.

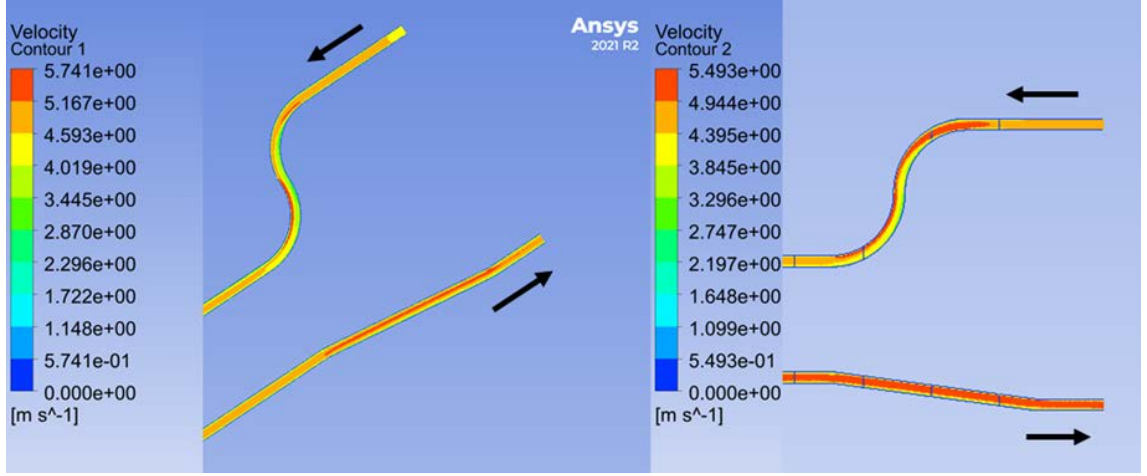


Figure 9.5: Velocity profile results at inlet and outlet boundaries from FLUENT (left) vs ANSYS CFX (right).

These differences could be attributed to reasons mentioned earlier. There could also be factor such as the mesh characteristics. Further, it should be noted that the ANSYS CFX results represent the state reached after twenty-thousand iterations whereas for FLUENT, five-thousand iterations were used. This does not mean that ANSYS CFX simulation results are not accurate enough at lower number of iterations, in fact, based on the residual plots of ANSYS CFX as presented on Appendix C, even a thousand iterations are acceptable enough for ANSYS CFX. It is beyond the scope of this thesis to decide which CFD software is more accurate. However, looking at the values of the considered parameters, this question is irrelevant as the numerical results are not significantly different from each other.

## 9.4 $^{16}\text{N}$ estimation

The fraction of  $^{16}\text{N}$  that decays when the activated fluid from the model enters the loop near the reactor core mirror loop, which has the same configuration, except it does not have a source is estimated using the equations:

$$N_o^m = N_2^i e^{-\lambda t}, \quad (9.1)$$

$$t = L/U, \quad (9.2)$$

where  $L$  is the total length travelled by the fluid and  $U$  is the average velocity throughout the model. The total length is estimated using the data presented in Appendix A. Average velocity is calculated using a separate simulation without the

additional variable. Table 9.3 presents the parameters used in the  $^{16}\text{N}$  estimation.

Table 9.3:  $^{16}\text{N}$  estimation parameters.

Parameter	Value
Total travelled length $L$	7.5906 [m]
Average velocity $U$	1.7567 [m/s]
time $t$	4.321 [s]

From these values, the percent decay along the mirror model could be estimated. Subsequently, the percentage of outgoing fluid from the model re-entering the inlet (stage 3) after circulating the mirror loop (stage 2), could be calculated as a multiplier (Equation 7.6):

$$multiplier = 1 - \left( \frac{N_2^i - N_o^m}{N_2^i} \right).$$

Table 9.4: Results for  $^{16}\text{N}$  decay calculation.

Parameter	Estimation	Simulation
Stage 1 outlet/ stage 2 inlet, $N_2^i$	1.3509E11 [ $m^{-3}$ ]	1.3509E11 [ $m^{-3}$ ]
Stage 2 outlet, $N_o^m$	8.8761E10 [ $m^{-3}$ ]	8.8806E10 [ $m^{-3}$ ]
multiplier	0.6570	0.6574

Table B.1 presents a comparison of results for  $^{16}\text{N}$  decay calculation between the simulation and the analytical calculation using the equation 9.1. A good agreement can be observed. From these values, it is shown that around thirty-four percent of  $^{16}\text{N}$  entering the mirror loop decays. Hence, sixty-six percent is expected to re-enter the model loop as a feed. Furthermore, it could be confirmed that the simulation for additional variable is accurate, at least compared to the values calculated using analytical calculation.

# Chapter 10

## Conclusions

In this thesis, a CFD analysis of the proposed new water activation/irradiation loop for the TRIGA research reactor using the ANSYS CFX has been performed. A prior study deemed the use of radial irradiation port as more feasible and is hence used in this work. Using ANSYS CFX, parameters such as pressure and velocity, which are vital for the irradiation loop, were analyzed via simulation. An acceptable mesh quality is applied to the model consisting of skewness of 0.2, orthogonal quality of 0.8 and eight (8) million elements, and  $y^+$  values within the acceptable range for the SST model used. Using a water mass flow rate of 1 kg/s, a pressure drop of 74 kPa and maximum velocity of 5.5 m/s were calculated for one half of the irradiation loop.

The  $^{16}\text{N}$  concentration behavior in the model was also analyzed in the form of an additional variable introduced to ANSYS CFX. The reaction rates for TRIGA at full power calculated from a prior study were used. Overall, the water activation loop is computed to have a maximum  $^{16}\text{N}$  concentration of  $2.95 \times 10^{11} \text{ m}^{-3}$  and an average of  $2.38 \times 10^{11} \text{ m}^{-3}$  at the outlet.

Verification of the simulation results were also conducted by analyzing the residuals and imbalances, particularly the erratic behavior for the additional variable which led to conducting up to twenty-thousand iterations. For validation purpose, additional simulations with the FLUENT code were performed demonstrating a rather good agreement with the thermo-hydraulic results of ANSYS CFX. Further, the estimation of  $^{16}\text{N}$  decay values is conducted by means of analytical calculations and the results are on par with those from the simulations.

Based on all of this, the results are deemed acceptable. These results could be used as reference for the construction of the actual design, contributing to factors such as design and operating limits in terms of pressure and velocity. Further, the  $^{16}\text{N}$  concentrations calculated could be a basis for future experiments, activities, and studies to be conducted on the proposed facility.





# Chapter 11

## Recommendations

A mesh refinement study dedicated to the model used in this thesis would be essential to exclude uncertainties related to the discretization. Testing different turbulence models would also be a beneficial contribution to the pool of knowledge regarding this area. Moreover, as this thesis only focused on the use of ANSYS CFX as an analysis tool, a more thorough investigation by comparison of  $^{16}\text{N}$  concentrations in the loop with the results from other dedicated code, specifically designed for calculation of reaction rates and decay of activation products will be beneficial in the future.



# Bibliography

- [1] *Description of TRIGA Reactor* (2014), [view 20. 6. 2022].
- [2] A. Žohar, A. Pungerčič, K. Ambrožič, V. Radulović, A. Jazbec, S. Rupnik, I. Lengar and L. Snoj, *Conceptual Design of Irradiation Facility with 6 MeV and 7 MeV Gamma Rays at the JSI TRIGA Mark II Research Reactor*, EPJ Web Conf. 225, 04014 (2020).
- [3] D. Kotnik, K. Pahor, L. Snoj and I. Lengar, *A Parametric Analysis of the Closed-Water Activation Loop at the JSI TRIGA Reactor* (2021), [view 20. 7. 2022].
- [4] ANSYS Inc, *ANSYS Meshing User's Guide 13.0* (2010), [view 07. 2. 2022].
- [5] M. B. Chadwick, P. Obložinský, et al., *ENDF/B-VII.0: Next generation evaluated nuclear data library for nuclear science and technology*, Nucl. Data Sheet 107(2006)2931 .
- [6] D. Green and R. Perry, *Perry's Chemical Engineers' Handbook. 9th edition* (McGraw Hill, 2018).
- [7] A. Žohar, A. Pungerčič, K. Ambrožič, V. Radulović, I. Lengar and L. Snoj, *Analysis of irradiation experiments with activated water radiation source at the JSI TRIGA Research Reactor*, Fusion Engineering and Design **161** (2020).
- [8] M. Stepišnik, B. Pucelj, L. Snoj and M. Ravnik, *Activity Analysis of Primary Coolant in TRIGA MARK II Research Reactor* (2009), [view 20. 6. 2022].
- [9] M. Stepišnik, *Analiza aktivnosti primarnega hladila pri delovanju raziskovalnega reaktorja TRIGA MARK II*, Magistrsko delo. Faculty of Math and Physics. University of Ljubljana. (2008).
- [10] A. Žohar and L. Snoj, *Analysis of the Primary Water Activation in a Typical PWR* (2016), [view 20. 6. 2022].
- [11] ANSYS Inc, *ANSYS CFX – Solver Theory Guide 14.0* (2011), [view 07. 2. 2022].
- [12] ANSYS Inc, *ANSYS CFX Tutorials 13.0* (2010), [view 07. 2. 2022].
- [13] D. Kotnik, A. Basavaraj, I. Lengar and L. Snoj, *Analysis of water activation loop at the JSI TRIGA research reactor* (2022), [view 18. 9. 2022].
- [14] LEAP Australia, *Understanding the physics of boundary layers*, Retrieved from: [www.computationalfluidynamics.com.au](http://www.computationalfluidynamics.com.au) (2020).

- [15] D. Wilcox, *Turbulence Modelling for CFD. Third edition* (DCW Industries, Inc, 2006).
- [16] F. Menter, *Two-equation eddy-viscosity turbulence models for engineering applications*, AIAA Journal **32** (1994).
- [17] T. Goorley, *MCNP6.1.1-Beta Release Notes. LA-UR-14-24680* (2014), [view 11. 6. 2022].
- [18] D. Brown et al, *ENDF/B-VIII.0: The 8th Major Release of the Nuclear Reaction Data Library with CIELO-project Cross Sections, New Standards and Thermal Scattering Data*, Nuclear Data Sheets **148**, 1 (2018).
- [19] G. Žerovnik, M. Podvratnik and L. Snoj, *On normalization of fluxes and reaction rates in MCNP criticality calculations*, Annals of Nuclear Energy **63**, 126 (2014).
- [20] *Convergence criteria*, [view 20. 6. 2022].

# Appendix A

## Model Dimensions

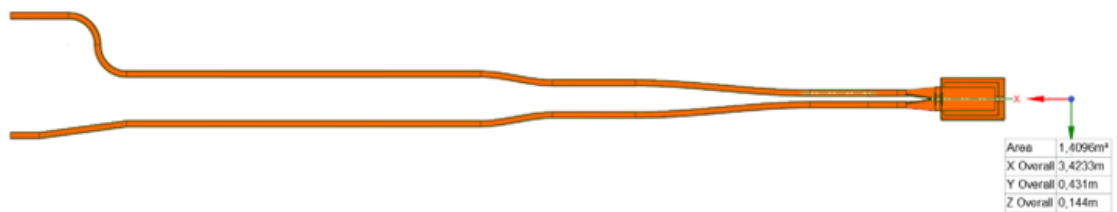


Figure A.1: Dimension of whole body.

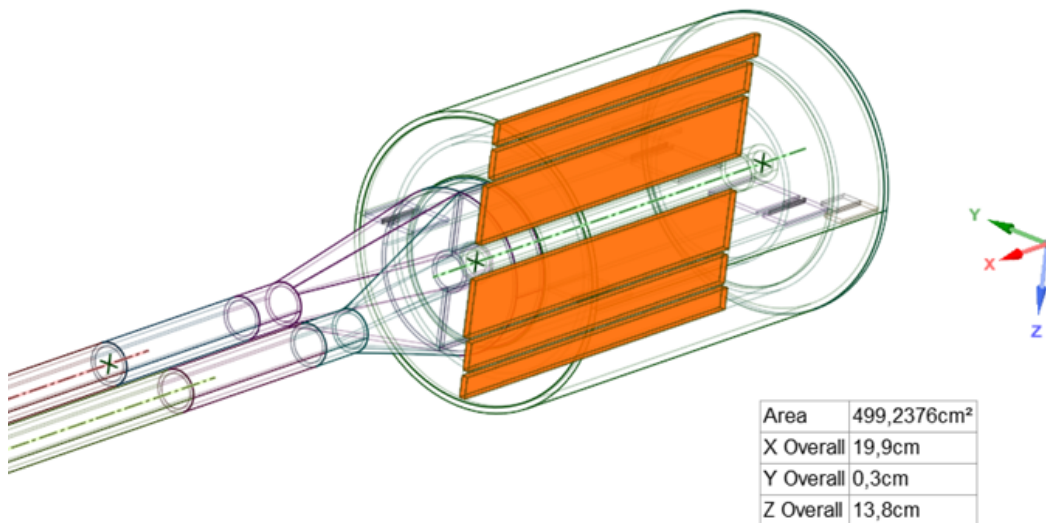


Figure A.2: Baffle dimensions.

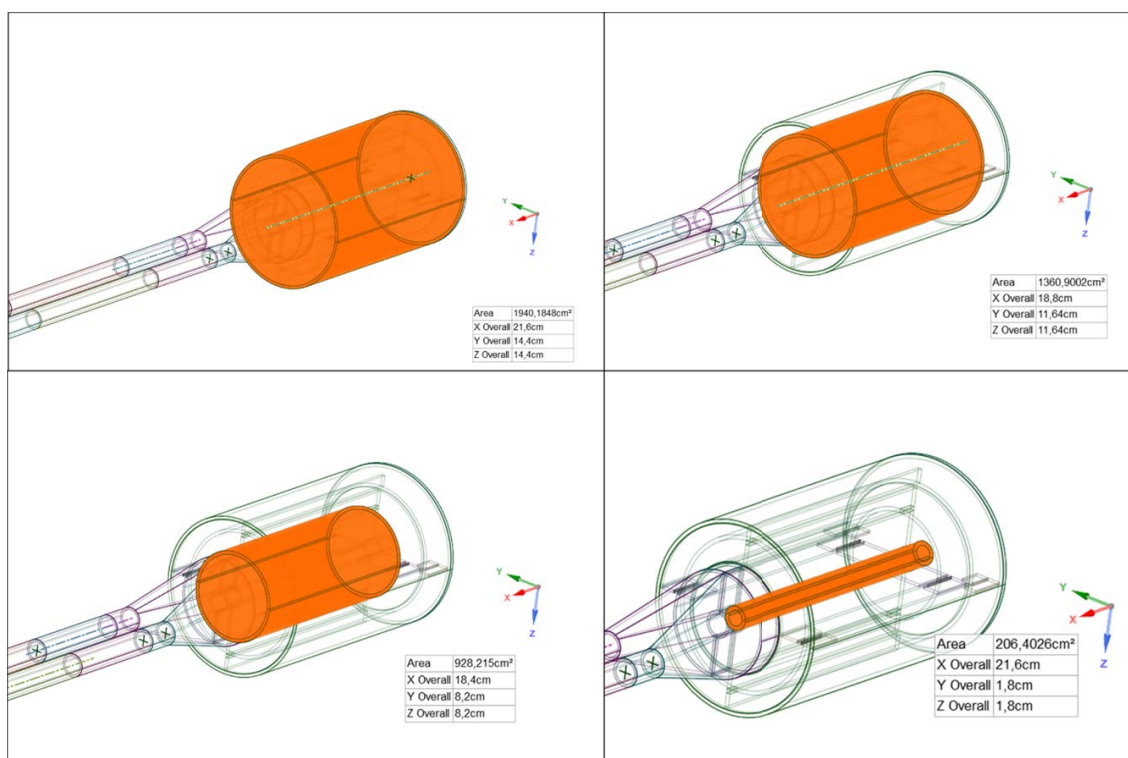


Figure A.3: Snail dimensions.

# Appendix B

## Mesh Settings

Table B.1: Results for  $^{16}\text{N}$  decay calculation.

Tab	Settings	Value
Mesh > Defaults	Physics Preference	CFD
	Solver Preference	Fluent
	Element order	Linear
	Element size	0.17213
Mess > Quality	Smoothing	Medium
Mess > Inflation	Automatic inflation	None
Body Sizing	Scoping method	Geometry selection (all bodies)
	Element size	0.002 m
Inflation	Scoping method	Geometry selection (fluid domain)
	Inflation option	First layer thickness
	First layer height	2E-4 m
	Maximum layers	7
	Growth rate	1.2

### *Skewness*

Skewness is one of the primary quality measures for a mesh. Skewness determines how close to ideal (i.e., equilateral or equiangular) a face or cell is as shown in Figure B.1 [4]. It is the deviation between the optimal cell size and to the existing cell size.

Tables B.2 and B.3 in Appendix B present the skewness and orthogonal quality limits criteria for the mesh, respectively. In order to meet these criteria, aside from meshing using the mesh default settings, additional techniques such as body sizing

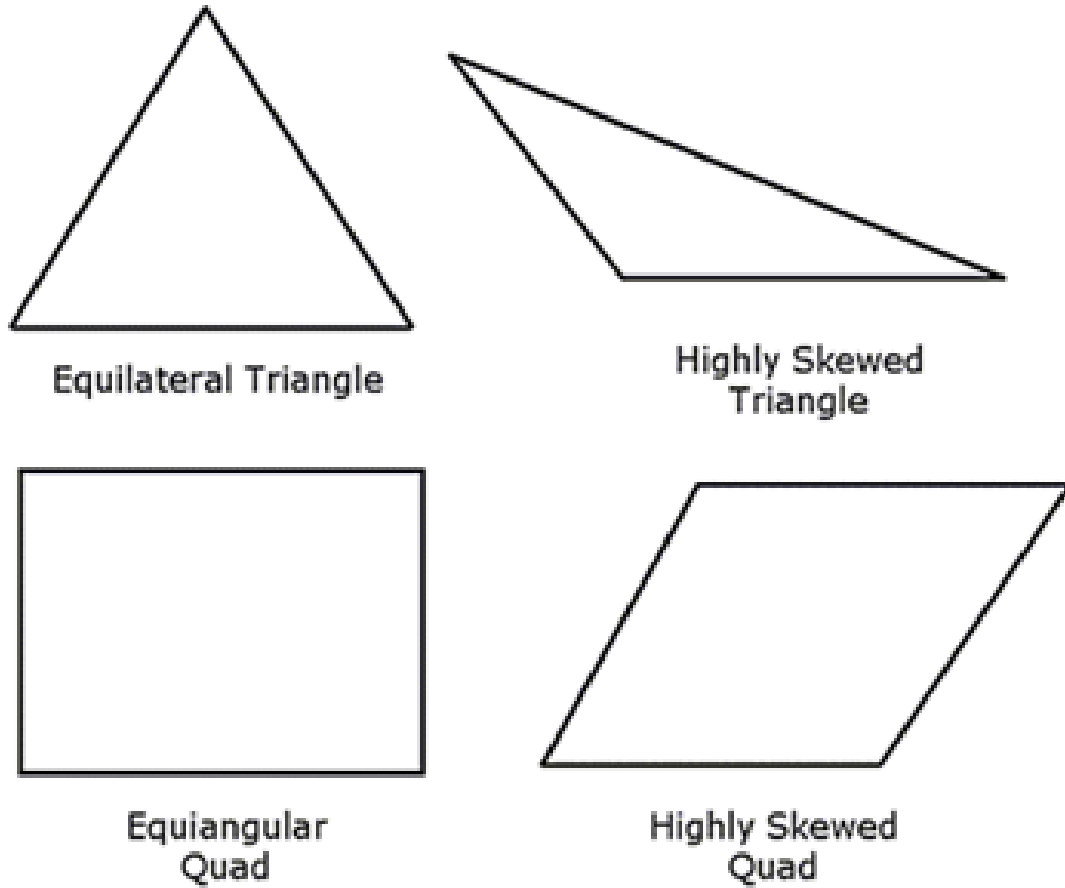


Figure B.1: Ideal and skewed triangles and quadrilaterals [4].

and inflation is employed.

Table B.2 presents the skewness values and the corresponding cell quality. A value of 0 indicates an equilateral cell (ideal) and a value of 1 suggests a completely degenerate cell (worst). Highly skewed cells are not preferred due to the poor accuracy they cause within the interpolated regions.

Based on Table B.2, the skewness value of the mesh model falls under the best (0) to excellent (0.202) cell quality category. The maximum skewness value of 0.939 registered indicates some bad (sliver) cell or one on which there are nodes that are nearly coplanar. Figure B.2 presents a plot of the mesh volume against the skewness.

From Figure B.2, the percent mesh volume (number of elements) can be visualized against the value of skewness. From this, it could be confirmed that the skewness values falls within acceptable range. Moreover, cells appearing beyond poor skewness value range were inspected as presented on Figure B.3.

Figure B.3 presents the location of the problematic cell with a sliver quality. Further inspection shows that this is just a single cell positioned right where the model is split at the baffle and wherein a void (for future detector installation) is located.



Table B.2: Skewness values and cell quality [4].

Skewness Value	Cell Quality
1	Degenerate
$0.9 - <1$	Bad (sliver)
$0.75 - 0.9$	Poor
$0.5 - 0.75$	Fair
$0.25 - 0.5$	Good
$>0 - 0.25$	Excellent
0	equilateral

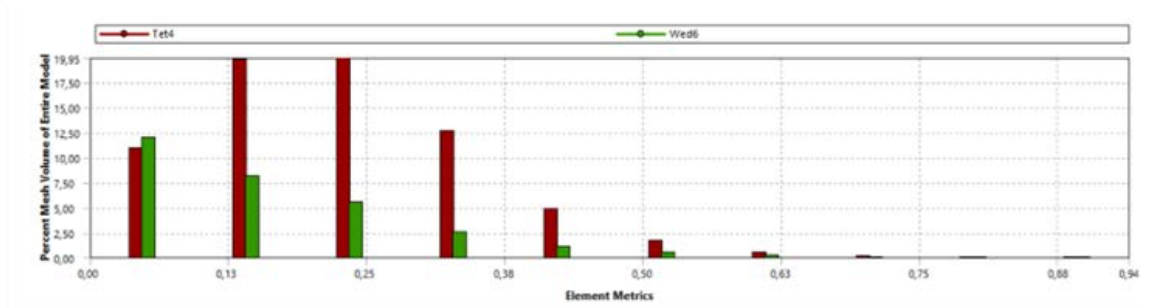


Figure B.2: Percent mesh volume of entire model vs skewness (*Tet4* = 4 Node Linear Tetrahedron; *Wed6* = 6 Node Linear Wedge [Prism]).

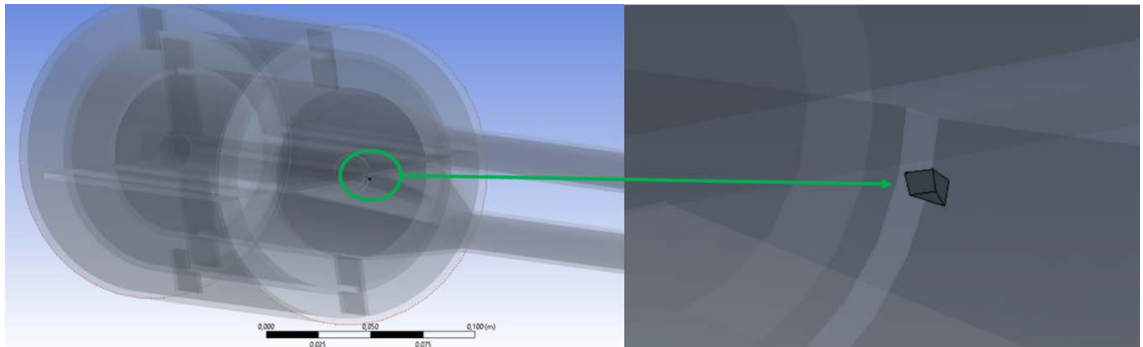


Figure B.3: Location of bad (sliver) mesh cell with maximum skewness.

Hence, this could be safely ignored as it does not affect the simulation and would not cause convergence problems.

#### *Orthogonal quality*

Orthogonal quality describes the closeness of the angles between adjacent element

## Appendix B. Mesh Settings

faces (or adjacent element edges) are to some optimal angle (depending on the relevant topology). The range of orthogonal quality is 0 to 1, where a value of 0 is the worst and a value of 1 is the best.

Table B.3: Orthogonal Quality Limits [4].

Smoothing Option	Orthogonal Quality Limit (without Inflation)	Orthogonal Quality Limit (with Inflation)
Low	0.1	0.01
Medium	0.15	0.05
High	0.2	0.1

Table B.3 presents the orthogonal quality minimum values according to the smoothing options and presence or absence of inflation feature. The smoothing option attempts to improve element quality by moving locations of nodes with respect to surrounding nodes and elements. For the case of the model used herein, medium smoothing option is used, and the inflation option is turned off.

Based on Table B.3, the orthogonal quality value of the mesh model as acceptable ( $>0.15$ ) and the mesh appears to be at good quality with values averaging 0.795 and maximum value reaching 1. A minimum orthogonal quality value of 0.002 is registered. Figure B.4 presents a plot of the mesh volume against the orthogonal quality.

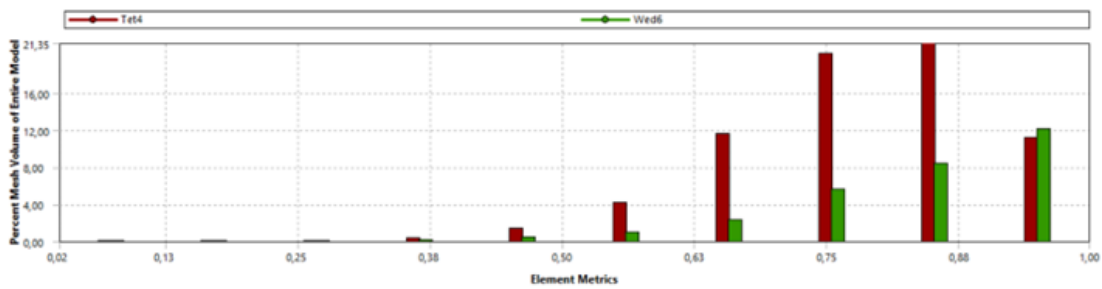


Figure B.4: Percent mesh volume of entire model vs orthogonal quality (*Tet4* = 4 Node Linear Tetrahedron; *Wed6* = 6 Node Linear Wedge [Prism]).

From Figure B.4, the percent mesh volume (number of elements) can be visualized against the orthogonal quality value.. From this, it could be confirmed that the orthogonal quality values falls within the acceptable range. Moreover, cells appearing below the orthogonal quality limit of 0.15 were inspected as presented on Figures B.5 and B.6.

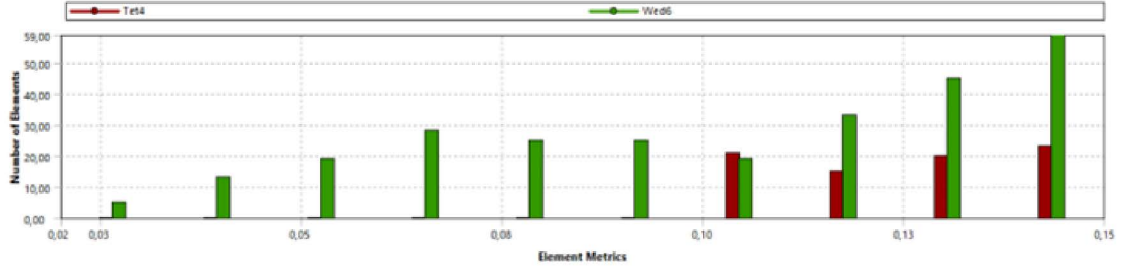


Figure B.5: Number of elements vs orthogonal quality for cells below orthogonal quality value limit of 0.15 (*Tet4* = 4 Node Linear Tetrahedron; *Wed6* = 6 Node Linear Wedge [Prism]).

Figure B.5 presents the number of elements below acceptable orthogonal quality. These cells are calculated to be less than 360 or precisely just  $1.34 \times 10^{-4}$  percent of the total mesh volume.

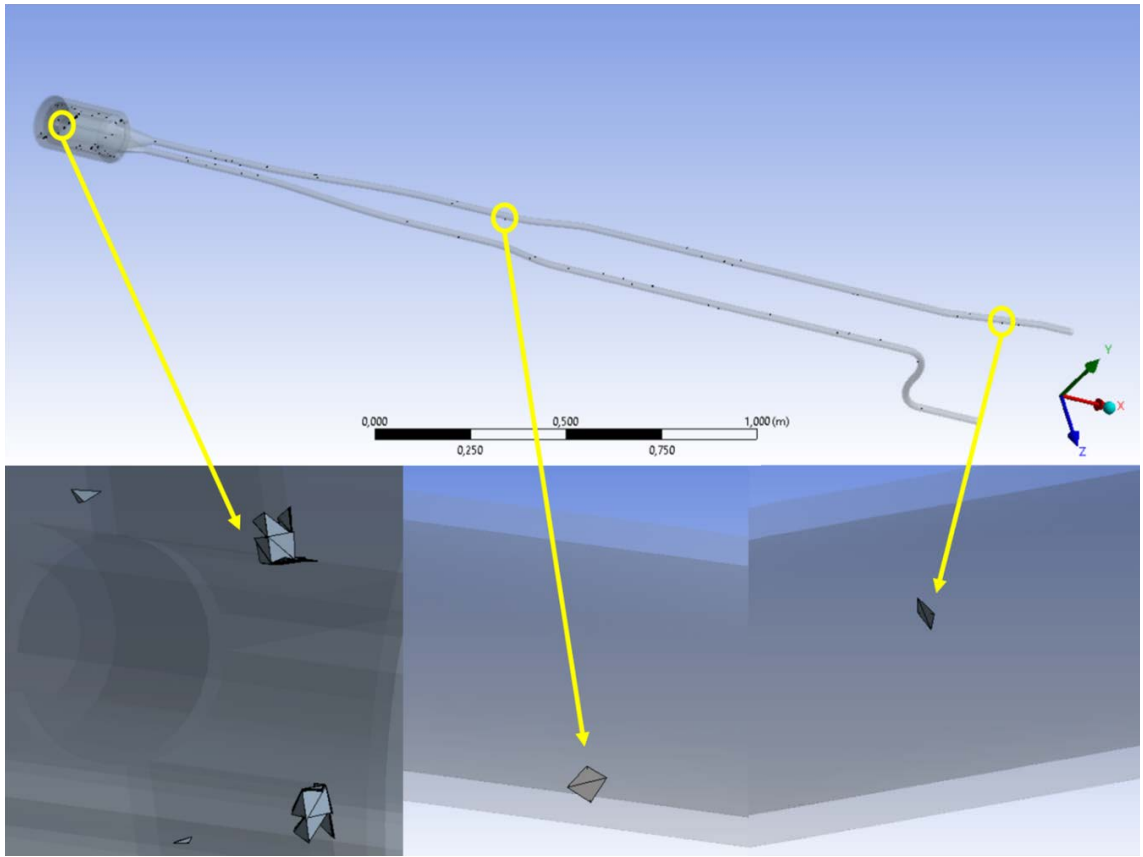


Figure B.6: Location of mesh cells with orthogonal values below the limit ( $<0.15$ ).

Figure B.6 presents locations of the mesh cells as indicated in Figure B.5. Further inspection shows that these are merely cells scattered at random positions within the model. Moreover, there are no clusters of degenerated cells in isolated locations. For these reasons, and the fact that the percentage of these mesh cells is very low

and therefore insignificant, they could safely be ignored as they would very likely not affect the simulation and would not cause convergence problems.

# Appendix C

## Residuals

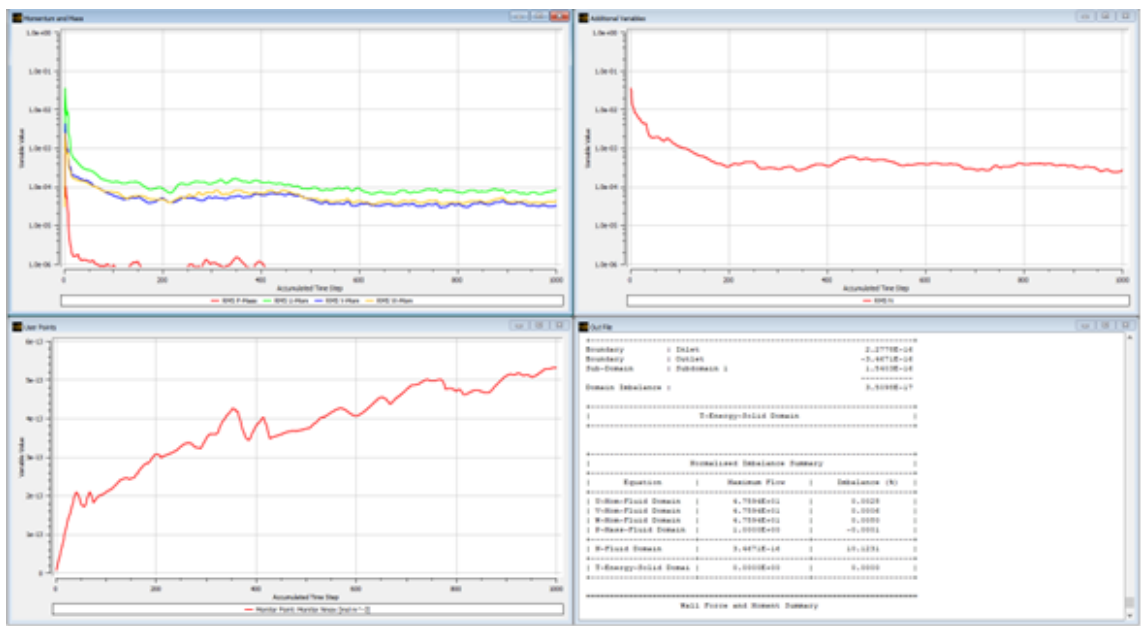


Figure C.1: Residuals plot for simulation at 1000 iterations.

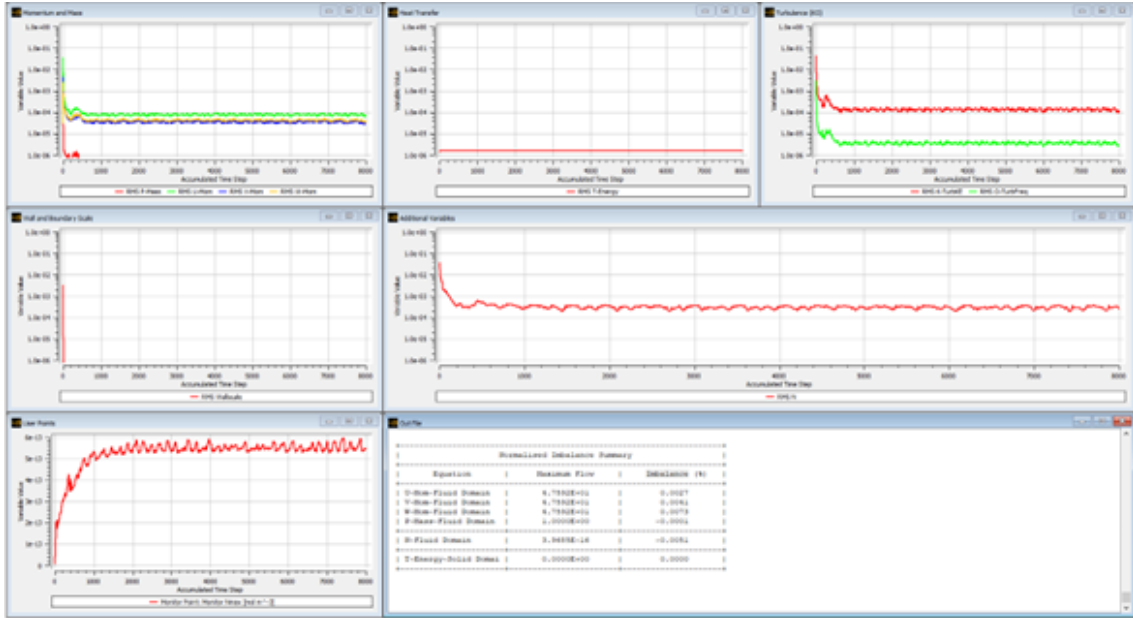


Figure C.2: Residuals plot for simulation at 8000 iterations.

# Appendix D

## Additional Variable Imbalance

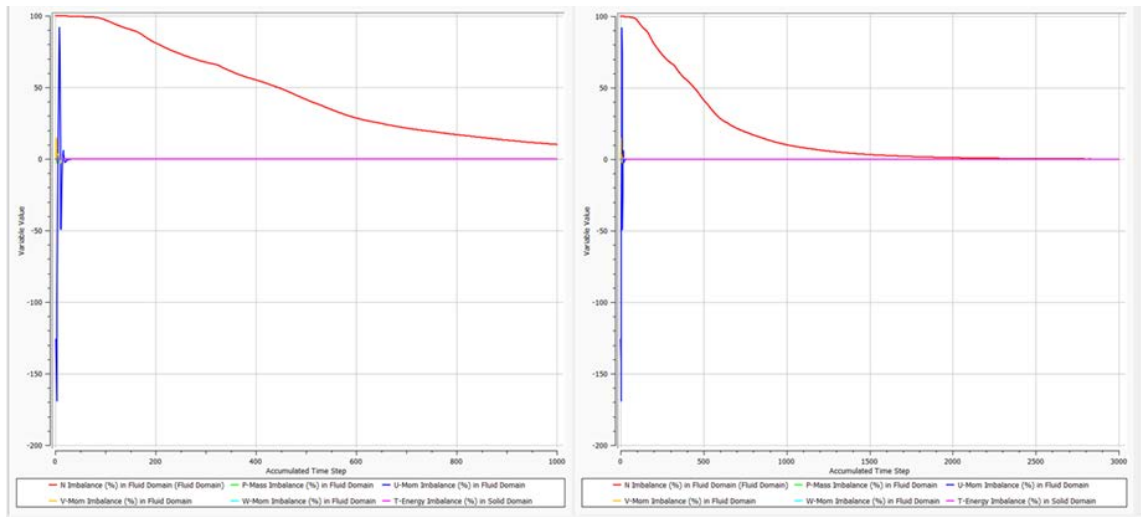


Figure D.1: Imbalance plot for N at 1000 (left) and at 3000 (right) iterations.

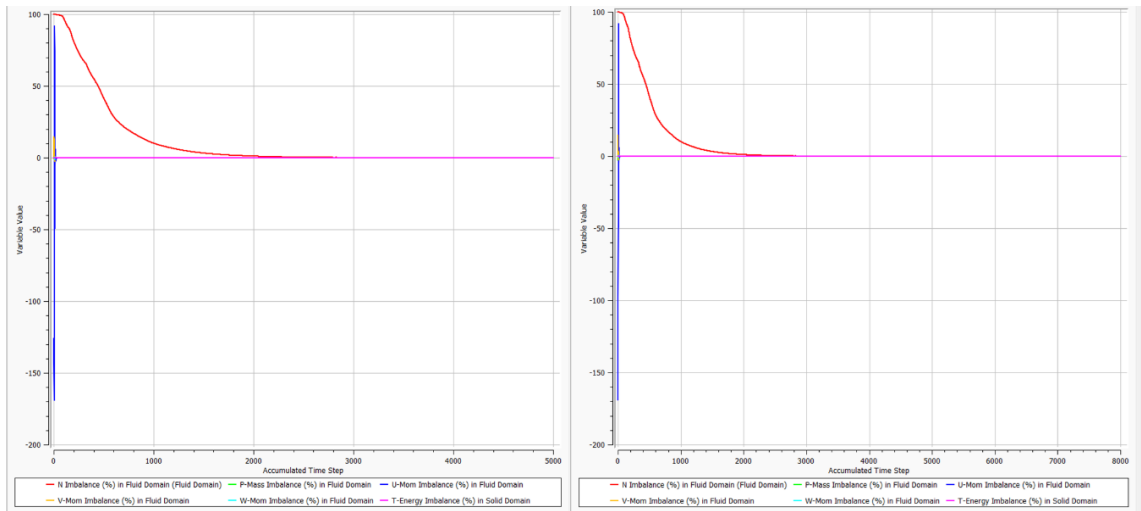


Figure D.2: Imbalance plot for N at 5000 (left) and at 8000 (right) iterations.

## Appendix D. Additional Variable Imbalance

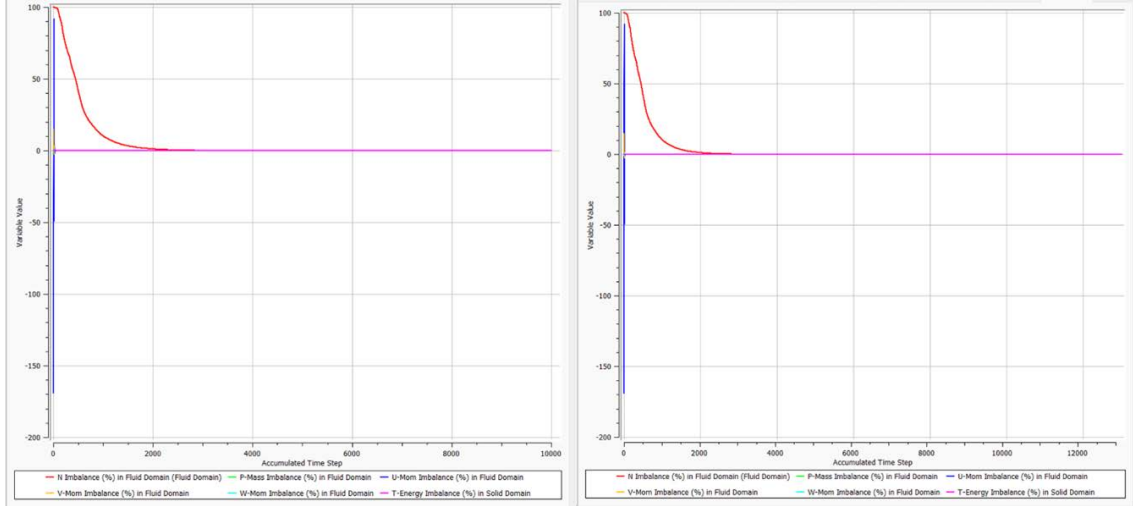


Figure D.3: Imbalance plot for N at 10000 (left) and at 13000 (right) iterations.

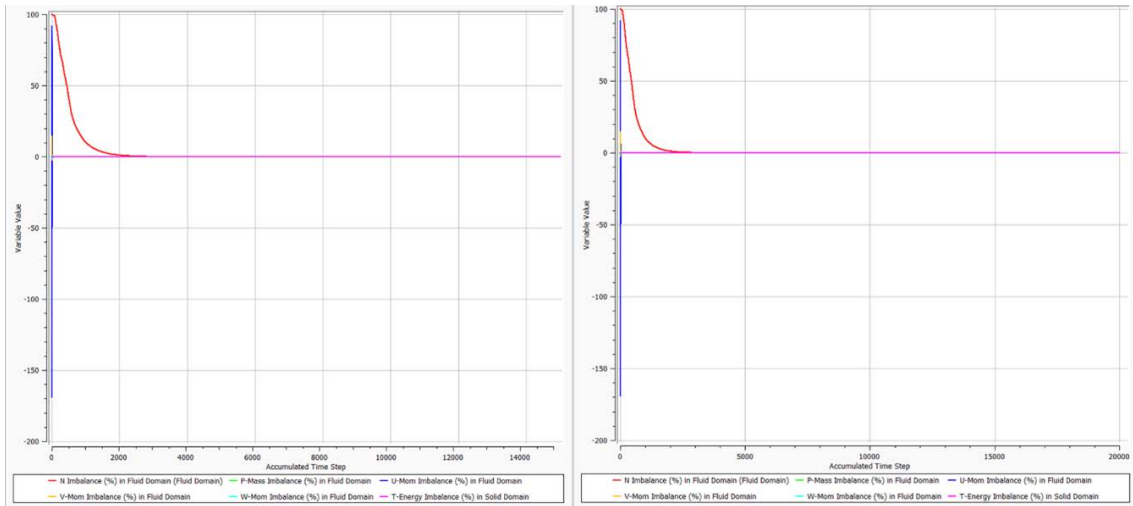


Figure D.4: Imbalance plot for N at 15000 (left) and at 20000 (right) iterations.



# Razširjeni povzetek v slovenskem jeziku

Voda s katero hladimo fuzijske in fisijske reaktorje je lahko izpostavljena večji količini nevtronov in se pri tem aktivira. Sevanje zaradi aktivacije vode lahko povzroči poškodbe električnih komponent in poveča prejeto dozo za osebje. Ker obstaja le malo virov gama žarkov z energijami v območju med 6 in 7 MeV, za preučevanje pojava na raziskovalnem reaktorju TRIGA Mark II na Institutu »Jožef Stefan« predlagajo obsevalni sistem z uporabo aktivirane vode kot vira gama žarkov. Predlagana je zasnova obsevalne zanke, ki je vstavljena v radialno odprtino raziskovalnega reaktorja. V zaprti zanki bo voda krožila od roba reaktorske sredice (aktivacijski del) do obsevalnega dela, ki se nahaja v zunanjem delu zanke izven radialne odprtine reaktorja. Za uspešno delovanje zanke sta potrebna zadosten pretok hladila in nadzor tlaka. Potrebna je tudi ocena vira žarkov gama.

Zaradi navedenih razlogov smo izvedli analizo obsevalne zanke s pomočjo programa za računalniško dinamiko tekočin ANSYS CFX. Pri aktivaciji vode nastanejo aktivacijski produkti, zlasti izotop dušika  $^{16}\text{N}$ , ki nastane pri jedrski reakciji kisikovega izotopa  $^{16}\text{O}$  z nevtroni. Ključne ugotovitve te študije so predstavljene na slikah 11.5, 11.6, in 11.7, kjer so prikazani rezultati porazdelitve tlaka, hitrosti in koncentracije izotopa  $^{16}\text{N}$  v polovici zanke, ki vključuje aktivacijski del znotraj radialne odprtine reaktorja. Pri masnem pretoku vode 1 kg/s sta izračunana padec tlaka 74 kPa in največja hitrost 5.5 m/s. Obnašanje koncentracije  $^{16}\text{N}$  smo v modelu analizirali s pomočjo dodatne spremenljivke uvedene v program ANSYS CFX. Kot vhodni podatek smo uporabili hitrosti reakcij za reaktor TRIGA pri polni moči, izračunanih iz predhodne študije [3]. Največja izračunana koncentracija  $^{16}\text{N}$  v zanki je  $2.95 \times 10^{11} \text{ m}^{-3}$ , povprečna vrednost na izstopu iz polovice zanke pa je  $2.38 \times 10^{11} \text{ m}^{-3}$ .

Rezultate smo preverili z analizo ostankov in neravnovesij. Izvedene so bile dodatne simulacije s programom ANSYS FLUENT, ki so pokazale razmeroma dobro ujemanje z izračuni programa ANSYS CFX. Poleg tega smo s pomočjo analitičnega izračuna ocenili razpad dušika  $^{16}\text{N}$  v zanki, in dosegli dobro ujemanje z rezultati simulacij.

Na podlagi izvedene analize sklepamo, da so rezultati simulacij sprejemljivi. Izračunani rezultati porazdelitev tlaka in hitrosti so lahko uporabni za načrtovanje in dejansko izdelavo zanke in omogočajo določitev projektnih in obratovalnih omejitev tlačnega padca in hitrosti. Prav tako lahko izračunane koncentracije dušika  $^{16}\text{N}$  uporabimo kot referenco za prihodnje zasnove eksperimentov in nadaljnje študije v predlagani obsevalni napravi.

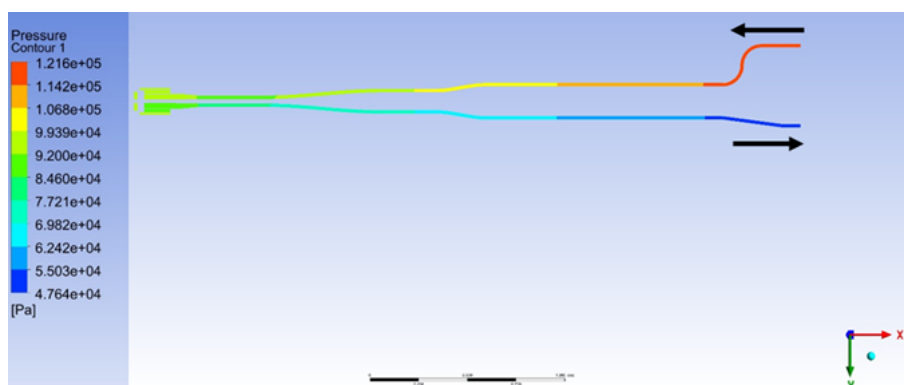


Figure 11.5: Porazdelitev tlaka v simulirani polovici zanke.

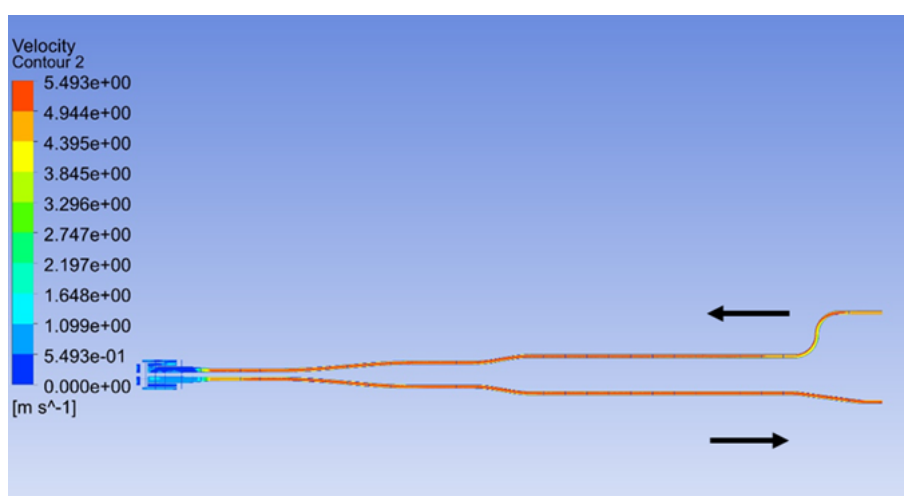


Figure 11.6: Porazdelitev hitrosti v simulirani polovici zanke.

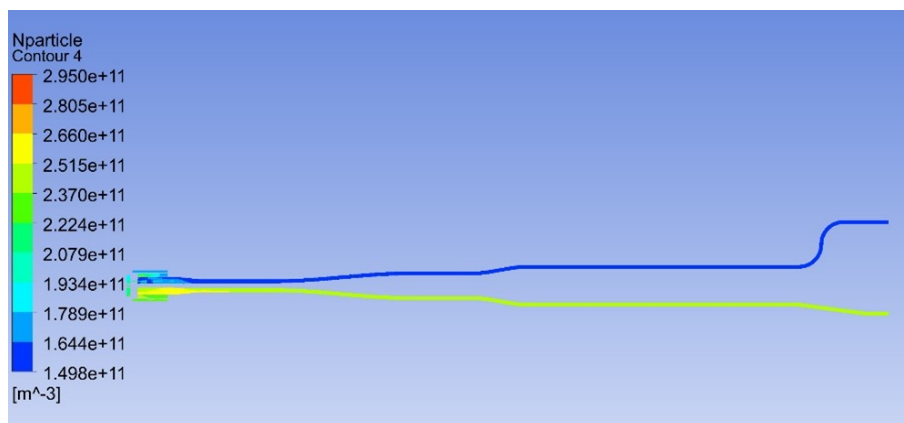


Figure 11.7: Porazdelitev koncentracije dušika  $^{16}\text{N}$  v simulirani polovici zanke.